TECHNISCHE UNIVERSITÄT DRESDEN

KZM on Si(1, 0, 0) Surface

Master-Arbeit
zur Erlangung des Hochschulgrades
Master of Science
im Master-Studiengang Physik

vorgelegt von

Andreas Weitzel
geboren am 10.08.1999 in Fulda

Institut für Theoretische Physik
Fakultät Physik
Bereich Mathematik und Naturwissenschaften
Technische Universität Dresden
2023

Eingereicht am xx. Monat 20xx

1. Gutachter: Prof. Dr. XX
2. Gutachter: Prof. Dr. YY

Summary

Abstract
English:

Abstract
Deutsch

Contents

1 Introduction

1.1 Motivation

In the area of semiconductor technology, silicon has become the cornerstone material driving the innovations that power our modern world. Its versatility, reliability, and abundance have solidified its position as the basic building block of the semiconductor industry, making silicon responsible for large parts of the recent human revolution. Its semiconducting properties facilitate the creation of wafers and integrated circuits, which are the centerpieces of computers, smartphones, and virtually any recent electronic device.

The most important part of integrated circuits are transistors. They function as switches which make up binary numbers and logic gates that every processor uses to do math. The speed at which processors perform calculations is majorly influenced by the number of transistors available. Therefore the pursuit of further miniaturization is crucial for performance enhancement. Up-to-date transistors approach wire diameters of about 5 nm. (reference?) This is close to atomic scales as the diameter of a silicon atom and the lattice constant are around 0.2 nm or 0.55 nm respectively. At these scales surface effects play an ever-increasing role in influencing the behavior and conductivity of the wires. Indeed manufacturers have difficulties controlling the current flow through the channels of the transistors. Hence a better understanding of the behavior of the surface is critical to ensure progress in classical computing.

Specifialy the Si(001) surface of monocrystalline silicon is important because it forms an interface with the oxide layer in transistors, that isolates silicon wires from their environment. Also wafers are cut along the Si(001) surface. The orientation of the cut is important since many of a crystal's structural and electronic properties are highly anisotropic.

The Si(001) surface undergoes an order-disorder phase transition between two surface reconstructions. While static properties like possible reconstructions, their energies and electronic structures are thoroughly investigated, the dynamic properties are not yet well understood. A rich dynamic phenomenon to consider is the Kibble-Zurek mechanism which describes the unavoidable non-adiabatic evolution of systems as they cross phase boundaries. The quench time is directly related to the number of domains of different order which in turn influence the

electronic properties of the surface.

1.2 Thesis Structure

This thesis aims to contribute to the understanding of the dynamic behavior of Si(001) during a quench. The already existing discrete Ising-like description of the surface is extended to a continuous XY-like model and adapted to the silicon surface. Well established molecular dynamics methods are used in combination with state-of-the-art parallel programming and GPU acceleration techniques to overcome the numerous numerical obstacles that are inherent to the nature of phase transitions. The used Langevin-type stochastic differential equations are motivated from a quantum mechanics point of view. Renormalization group techniques are employed to set a theoretical baseline for the investigation of the phase transition.

Chapter 2 firmly concludes the current viewpoint on and knowledge of the Si(001) surface and its order-disorder phase transition. Chapter 3 explores the renormalization group description of phase transitions to create a theoretical understanding for what follows. It introduces the concept of universality and the methods of finite size scaling which are used to investigate and interpret the simulation results. Chapter 4 explains the used numerics and motivates our description from a quantum point of view. Moreover, the XY model used to describe the Si(001) surface is introduced and investigated. The results of various investigations like dynamic quenches, but also static measurements are written in Chapter 5. In Chapter 6 the main points of the thesis are summarized and an outlook for possible further research is given. The appendix contains calculations to various parts of the work as well as benchmarks for the simulation.

The simulation is written in `C++` using `CUDA` [54] and `Thrust` [67]. The evaluation and plotting is done in `python`. The whole source code can be obtained at `github.com`.
The surface is semiconducting [28, 70, 26]

2 The Si(001) Surface

2.1 Surface Reconstruction

Below a temperature of $T = 1687$ K silicon crystallizes in a diamond cubic crystal structure as shown in Figure 2.1 with a lattice constant of $a = 5.431$ Å [68]. When cutting this crystal structure along the crystallographic (001) plane, the resulting system exhibits a surface reconstruction. Surface atoms are left in a high-energy state with two dangling bonds. One of those bonds can be invested into forming a dimer with the neighboring Si atom in (110) direction [15], which, as shown by theoretical calculations [61, 4, 16], leads to a large reduction of surface energy of roughly 1.8 eV per dimer.

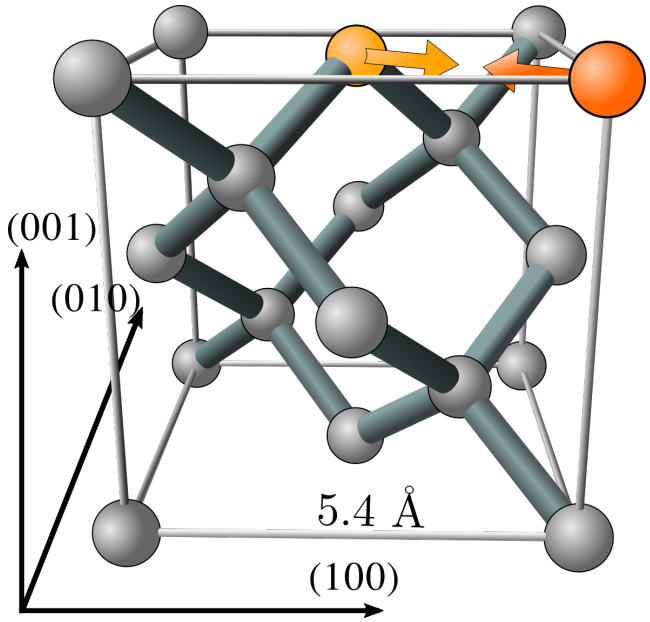

Figure 2.1: The crystalline structure of Si in its solid state is shown [5]. The orange colored atoms form a dimer when cutting the diamond structure along the (001) plane. The coordinate system axis are denoted by their Miller indices and normal to their corresponding crystallographic planes. The orange silicon atoms dimerize during reconstruction of the (001) surface.

The resulting dimers can further reduce their energy by vertical buckling. The dimers tilt to an angle of about 18° [61, 57], which lowers the surface energy by another 0.15 eV [31] per dimer. A charge transfer of approximately $0.1e$ [11, 43] is induced by the buckling. The electrostatic interaction of the dimers is characterized by a coupling strength J. The surface reconstruction

with the lowest energy was through theoretical [61, 57, 31, 11] and experimental (low energy electron diffraction [48, 40, 11] and scanning tunnel microscope [72, 69]) methods found to be the $c(4\times2)$ reconstruction, shown in Figure 2.2 (b). It minimizes the interaction energy as well as the surface stress. The alternative buckling in both directions suggests an antiferromagnetic interaction along (110), $J_{\|}$, and across $(1\bar{1}0)$, $J_{\perp}$, the dimer rows, but the interaction across the row is actually ferromagnetic. However, the dimer interactions are strongly anisotropic with $J_{\|}$ being much larger than $J_{\perp}$ which causes a guaranteed alternating buckling in (110) direction. The ferromagnetic diagonal interactions $J_{\times}$ overpower $J_{\perp}$ so diagonal alignment is preferred, which in turn implies anti-alignment in $(1\bar{1}0)$ direction. It has been suggested that the interaction is of dipole kind [57].

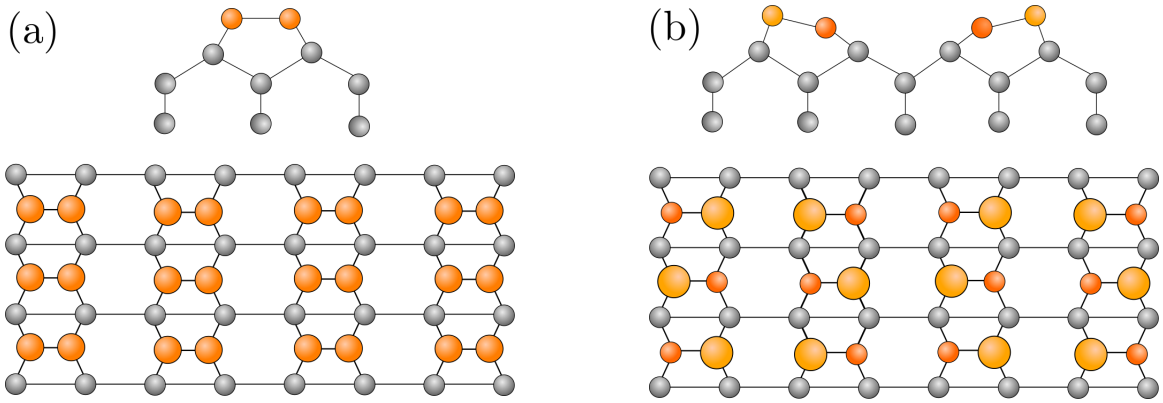

Figure 2.2: (a) The formation of dimers results in the symmetric $p(2\times1)$ reconstruction and saves a large amount of 1.8 eV per dimer compared to the ideal $p(1\times1)$ structure. **(b)** The dimers are unstable to vertical buckling. The buckling pattern that was found to have the lowest surface energy is the $c(4\times2)$ reconstruction.

2.2 Phase Transition of the Si(0,0,1) Surface

The Si(001) surface exhibits an order-disorder phase transition from the disordered $p(2\times1)$ phase shown in Figure 2.2 (a) to the ordered $c(4\times2)$ reconstruction at a critical temperature of about $T_c \approx 200$ K [66]. This continuous phase transition will be of central importance in the following discussion. The $p(2\times1)$ structure is short term for the disordered phase since fast flipping of the dimers at a frequency of about 10^{-11} Hz let the system appear to be in the $p(2\times1)$ state at high-temperature measurements.

The strong anisotropy leads to long streaks of order along the dimer rows ($\|$) and short domains of order across the dimer rows ($\perp$) . Brand et. al [10] found that the ratio of correlation length amplitudes ξ^+ is $\xi^+_{\|}/\xi^+_{\perp} \approx 5.2$. The lattice spacing along the dimer rows is $a_{\|} = 3.84$ Å, while it is $a_{\perp} = 2a_{\|} = 7.68$ Å across.

To understand the phase transition of the Si(001) surface we need to have a general knowledge of phase transitions.

3 Phase Transitions

The term phase transition describes the process of transition between states of a system by changing an external parameter, like pressure p or temperature T. Common types are transitions from an unordered to an ordered state after cooling a system below its critical temperature T_c like the transition from paramagnets to ferromagnets. Intuitively the transitions happen as a result of free energy $F = U - TS$ minimization. At high temperatures entropy S dominates, leading to unordered states, but at low temperatures the impact of the internal energy U takes over. The minimization of U usually leads to a form of ordering dictated by the microscopic Hamiltonian.

Mathematical definition:
Let N denote the number of components, or equivalently the number of lattice sites, and V the volume of the system in question. The **thermodynamic limit** $N \to \infty$ and $V \to \infty$ describes the limit to infinitely large systems while keeping the density N/V constant. For a system dependent on a set of coupling constants $[K]$ the free energy per site f is defined as

$$f[K] = \lim_{N\to\infty} \frac{F[K]}{N} \ . \tag{3.1}$$

With f a precise definition of the phase boundary is possible. The d coupling constants $[K]$ span the so called phase space. In this d-dimensional phase space, the free energy density f is analytic almost everywhere except from the possibility of non-analyticities at certain points, lines, planes, etc. up to dimensionality $d-1$. The connected areas of analyticity are called **phases** and non-analyticitys with dimension $d-1$ are called **phase boundaries** or **critical manifolds**. Since f has to be continuous everywhere, the phase boundaries come in two classes:

1. at least one of the first derivatives $\frac{\partial f}{\partial K_i}$ is discontinuous across the phase transition. This case belongs to the **first-order phase transition**.
2. all derivatives $\frac{\partial f}{\partial K_i}$ are continuous. This transition is called the **continuous phase transition**.

The phase transition of the silicon surface belongs to the continuous phase transitions. As the thermodynamic limit is never obtained, descriptions using f are not always reliable. Using the correlation length ξ, which simply put describes the spatial extent of fluctuations in the

system, a criterion for accurate predictions can be given. If the system size L is much greater than the correlation length $\xi \ll L$ the considered system can be expected to behave according to the ideal behavior described by f.

Phase transitions exhibit rich phenomena like the divergence of the correlation length ξ at the critical point. The reason for the universality of this behavior across different systems will be outlined in the next section with the help of renormalization group theory.

3.1 Renormalization Group Considerations

The renormalization group (RG) theory is a general framework to study phase transitions and particle physics. It employs scale invariance arguments, meaning the self-similarity characteristics of systems at different length scales, to investigate their properties. In the following basic considerations as well as important results shall be presented briefly.

Consider an infinite two-dimensional $d = 2$ lattice with Ising-like spins s_{mn} on each site. The site is denoted by a tuple of indices (m, n). Following Kadanoff [35], we examine a square of length l in lattice spacing units a and map their combined l^2 spins to a single value S^l. This block spin is renormalized to ± 1 by taking on the value of the majority of spins. The obtained S^l_{ij} define a new Ising system, but on a different length scale with a new lattice spacing la like shown in Figure 3.1. The proposal is that there exists a set of coupling parameters $[K^l]$ defining the interaction of the block spins so that the total free energy stays the same. In terms of the free energy density we can write

$$f[K] = l^{-2} f[K^l] \ , \tag{3.2}$$

since the free energy density after the transformation has to increase by a factor l^2 as we measure in an l-times larger length scale. The same considerations are made for the correlation length, giving

$$\xi[K] = l\xi[K^l] \ . \tag{3.3}$$

Suppose we know how the coupling constants change under an RG transformation R_l

$$[K^l] = R_l([K]) \ . \tag{3.4}$$

This is the starting point to comprehend why phase transitions exhibit singular behavior. The

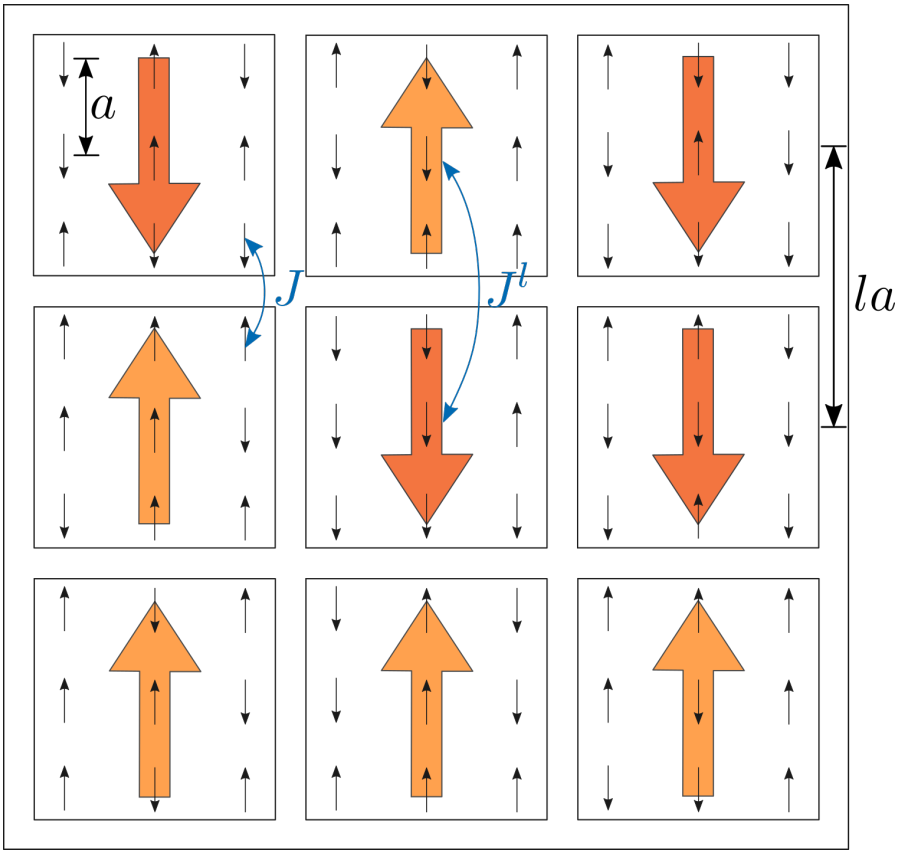

Figure 3.1: In Kadanoffs block spin picture, l^2 Ising-spins are combined to a composite spin that takes on the value of the majority of spins. The block spin is the standard example for a renormalization group transformation. Under the RG transformation, the relevant length scales change from a to la and the coupling strengths from J to $J^l = R_l(J)$.

idea is that even though the partition function

$$Z(\{K\}) = \sum_{\{s\}} e^{-\beta H(\{s\},\{K\})} \tag{3.5}$$

is a sum of exponentials which are analytic in $[K]$, the singularities can arise after an infinite number of RG iterations. Applying multiple RG transformations traces out a trajectory in coupling constant space $[K^{(l_1)}] \to [K^{(l_2)}] \to ... \to [K^{(l_n)}]$ the **RG flow**. This trajectory is almost always attracted to fixed points. The behavior of a system near a fixed point is the origin of scaling and lets us extract important information, like the shape of the phase diagram.

A fixed point of the RG map satisfies

$$[K^{(*)}] = R_l[K^{(*)}] \ . \tag{3.6}$$

At this point the correlation length transforms according to

$$\xi[K^{(*)}] = \xi[K^{(*)}]/l \ , \tag{3.7}$$

meaning that the correlation length either has to be 0 or ∞. The same is true for the free energy density. In proximity of a fixed point we write the initial coupling constants as

$$K_i = K_i^{(*)} + \delta K_i \qquad \text{and} \qquad K_i^l = R_l(K_i^{(*)} + \delta K_i) = K_i^{(*)} + \delta K_i^l \ . \tag{3.8}$$

The RG Transformation of K_i is in general dependent on all K so that

$$K_i^l = K_i^l[K] = K_i^l(K_1^{(*)} + \delta K_1, K_2^{(*)} + \delta K_2, ...). \tag{3.9}$$

The Taylor expansion of K_i^l around the fixed point $[K^{(*)}]$ yields the linearized RG Transformation

$$K_i^l = K_i^{(*)} + \sum_j \left.\frac{\partial K_i^l}{\partial K_j}\right|_{K_j = K_j^{(*)}} \delta K_j + O((\delta K_j)^2) = K_i^{(*)} + \delta K_i^l + O((\delta K_j)^2) \ . \tag{3.10}$$

Omitting terms quadratic in δK_j identifies

$$\delta K_i^l = \sum_j \left.\frac{\partial K_i^l}{\partial K_j}\right|_{K_j = K_j^{(*)}} \delta K_j \ . \tag{3.11}$$

We write down the partial derivatives as a matrix

$$M_{ij}^l = \left.\frac{\partial K_i^l}{\partial K_j}\right|_{K_j = K_j^{(*)}} \ , \tag{3.12}$$

and construct an eigenvalue problem

$$M^l k^{(\sigma)} = \lambda_l^{(\sigma)} k^{(\sigma)} \ , \tag{3.13}$$

where σ labels the eigenvalues. Because two consecutive RG Transformations by l_1 and l_2 have to yield the same result as one by $l_1 l_2$, we know that

$$M^{l_1} M^{l_2} = M^{l_1 l_2} \ , \tag{3.14}$$

implying that

$$\lambda_{l_1}^{(\sigma)} \lambda_{l_2}^{(\sigma)} = \lambda_{l_1 l_2}^{(\sigma)} \ . \tag{3.15}$$

Setting $l_2 = 1$ gives $\lambda_{l_1}^{(\sigma)} \lambda_1^{(\sigma)} = \lambda_{l_1}^{(\sigma)}$ which lets conclude that $\lambda_1^{(\sigma)} = 1$. Differentiating Equation 3.15 with respect to l_2 yields

$$\frac{\mathrm{d}}{\mathrm{d}l_2}\left(\lambda_{l_1}^{(\sigma)} \lambda_{l_2}^{(\sigma)}\right) = \lambda_{l_1}^{(\sigma)} \left(\frac{\mathrm{d}}{\mathrm{d}l_2} \lambda_{l_2}^{(\sigma)}\right) + \left(\frac{\mathrm{d}}{\mathrm{d}l_2} \lambda_{l_1}^{(\sigma)}\right) \lambda_{l_2}^{(\sigma)} = \left(\frac{\mathrm{d}}{\mathrm{d}l_2} \lambda_{l_2}^{(\sigma)}\right) \lambda_{l_1}^{(\sigma)} \tag{3.16}$$

for the left hand side and

$$\frac{\mathrm{d}}{\mathrm{d}l_2}\lambda^{(\sigma)}_{l_1 l_2} = \frac{\mathrm{d}}{\mathrm{d}(l_2 l_1)}\lambda^{(\sigma)}_{l_1 l_2}\frac{\partial}{\partial l_2}(l_1 l_2) = l_1\frac{\mathrm{d}}{\mathrm{d}(l_1 l_2)}\lambda^{(\sigma)}_{l_1 l_2} \tag{3.17}$$

for the right hand side. By setting $l_2 = 1$ the differential equation

$$\frac{\mathrm{d}}{\mathrm{d}l_2}\lambda^{(\sigma)}_{l_2}\bigg|_{l_2=1}\lambda^{(\sigma)}_{l_1} = y_\sigma\lambda^{(\sigma)}_{l_1} = l_1\frac{\mathrm{d}}{\mathrm{d}l_1}\lambda^{(\sigma)}_{l_1} \tag{3.18}$$

with

$$y_\sigma = \frac{\mathrm{d}}{\mathrm{d}l_2}\lambda^{(\sigma)}_{l_2}\bigg|_{l_2=1} \tag{3.19}$$

is obtained. A solution to Equation 3.18 is

$$\lambda^{(\sigma)}_l = l^{y_\sigma}\ , \tag{3.20}$$

with y_σ being independent of l. This is an important result on the way to show the origin of scaling. The $k^{(\sigma)}$ are vectors in the coupling constant space, so Equation 3.13 indicates that some δK_i grow and some shrink when applying RG transformations, depending on the eigenvalue $\lambda^{(\sigma)}_l$. Three cases are distinguished:

1. **Relevant** directions and eigenvalues: $|\lambda^{(\sigma)}_l| > 1$, meaning that $y_\sigma > 0$ and δK in direction of $k^{(\sigma)}$ grow.
2. **Irrelevant** directions and eigenvalues: $|\lambda^{(\sigma)}_l| < 1$, meaning that $y_\sigma < 0$ and δK in direction of $k^{(\sigma)}$ shrink.
3. **Marginal** directions and eigenvalues: $|\lambda^{(\sigma)}_l| = 1$, meaning that $y_\sigma = 0$ and δK in direction of $k^{(\sigma)}$ do not change.

After many iterations, only the relevant eigenvalues will be important, as shrinking δK_i won't impact the RG flow significantly. If we differ from the fixed point in a relevant direction, the differences to the fixed point will become larger and the RG transformation flow will move away from the fixed point. Deviations in irrelevant direction will flow into the fixed point.

A simplified understanding can be achieved for a system satisfying

$$\frac{\partial K^l_i}{\partial K_j}\bigg|_{K_j=K^{(*)}_j} = \delta_{ij}\frac{\partial K^l_j}{\partial K_j}\bigg|_{K_j=K^{(*)}_j}\ , \tag{3.21}$$

so that M^l_{ij} becomes diagonal and the eigendirections $k^{(\sigma)}$ point directly along the axes e^{K_i} of the phase space defined by K. If the eigenvalue $\lambda^{(\sigma)}_l$ to $k^{(\sigma)}$, parallel to e^{K_i}, is larger than one,

the coupling K_i will grow. In this case K_i would be a relevant coupling constant.

Consider a system with only one coupling constant, in this case the temperature, and choose T in the vicinity of a fixed point $T^{(*)}$. Apply a RG transformation to T and consider the difference

$$T^l - T^{(*)} = R_l(T) - T^{(*)} \ . \tag{3.22}$$

Using Equation 3.10 we can rewrite

$$R_l(T) = T^{(*)} + \delta T^l = T^{(*)} + \left.\frac{\partial T^l}{\partial T}\right|_{T=T^{(*)}} \delta T = T^{(*)} + \lambda_l \delta T \ , \tag{3.23}$$

since M^l has only one component and δT is therefore automatically in eigenvector direction. Equation 3.22 then becomes

$$\varepsilon^{(l)} = \lambda_l \varepsilon \overset{\text{Eq. 3.20}}{=} \varepsilon l^{y_\varepsilon} \ , \tag{3.24}$$

in terms of the **reduced temperature** $\varepsilon = \frac{T-T^{(*)}}{T^{(*)}}$. After n RG iterations this gives

$$\varepsilon^{(nl)} = (l^{y_\varepsilon})^n \, \varepsilon \ . \tag{3.25}$$

Now consider again how the correlation length transforms after n RG transformations

$$\xi(\varepsilon) = l^n \xi(\varepsilon^{nl}) = l^n \xi(l^{n y_\varepsilon} \varepsilon) \ . \tag{3.26}$$

Substituting $\tau = l^{n y_\varepsilon} \varepsilon$ into Equation 3.26 yields

$$\xi(\varepsilon) = \tau^{1/y_\varepsilon} \varepsilon^{-1/y_\varepsilon} \xi(\tau) \ , \tag{3.27}$$

showing that the correlation length diverges as $\varepsilon \to 0$. This is the origin of scaling and universality! Note that knowledge of a valid RG transformation R_l directly provides knowledge of y_ε via

$$y_\varepsilon = \frac{1}{l} \ln \left(\left.\frac{\partial R_l(T)}{\partial T}\right|_{T^{(*)}} \right) \ . \tag{3.28}$$

3.2 Universality and Static Scaling

The last section traced the origin of universality and scaling in phase transitions. This section will deal with the term universality and its implications in more detail.

Scaling laws like Equation 3.27 can be derived for different system quantities. In the context of phase transitions, **static scaling** means the power law dependence of a system quantity **in equilibrium**, like the correlation length ξ, on a coupling parameter, like the temperature T. The exponent of this power law is called the **critical exponent**. Some important scaling relations are shown in Table 3.1. Comparing the scaling law of ξ with Equation 3.27 identifies

$$\frac{1}{y_\varepsilon} = \nu \ . \tag{3.29}$$

The prefactors of the power laws are called the **critical amplitudes** and ν, α, etc. are the

Table 3.1: Some important scaling laws are summarized in the notation of [56]. The universal critical exponents α, β, etc. are the same above and below the phase transition. In contrary, the nonuniversal critical amplitudes may differ at different sides of the critical point. Hence, they are labeled with a superscript $\pm$. The dimensionality is denoted by d.

Name	Symbol	Scaling
specific heat	C_H	$T_c C_H \approx A^{\pm} \lvert\varepsilon\rvert^{-\alpha}$
order parameter	Ψ, M	$\lvert M\rvert \approx B \lvert\varepsilon\rvert^{-\beta}$
susceptibility	χ	$\chi \approx C^{\pm} \lvert\varepsilon\rvert^{-\gamma}$
correlation length	ξ	$\xi \approx f^{\pm} \lvert\varepsilon\rvert^{-\nu}$
two-point correlation function	$C(\vec{r})$	$C(\vec{r}) \propto \lvert\vec{r}\rvert^{-d+2-\eta}$

mentioned critical exponents. The superscript $\pm$ denotes whether the phase transition is approached from below $(-)$ or above $(+)$ the critical temperature T_c. The critical exponents are the same on both sides of the transition, but the amplitudes vary.

These scaling laws are only valid in the thermodynamic limit for $\varepsilon \to 0$ as the derivation in Section 3.1 assumed that the system is in the vicinity of a critical point. Otherwise they exhibit **corrections to scaling** that result out of irrelevant and marginal eigenvalues of the RG transformations as well as **finite-size** corrections.

Systems that share the same set of critical exponents belong to the same **universality class**. Section 3.1 showed that the exponents can be calculated solely from the RG transformation which suggests that systems with similar transformations exhibit similar critical behavior. Indeed it is found that the universality class of a system only depends on

- the **symmetry group** of the system Hamiltonian,
- the **dimensionality** of the problem,
- and whether the **interaction** between the components is **short-ranged**.

In contrast to the critical exponents, the critical amplitudes are not universal, but their ratios, for example f^+/f^-, are.

The concept of universality is very useful to investigate real systems at the critical point. As a result of scale invariance and self similarity, the microscopic dynamics of a system become irrelevant at $\varepsilon = 0$. Its behavior can then be approximated by a simplified, in the best case exactly solvable, model.

The extraction of critical exponents is notoriously difficult for various reasons, one being the inaccessibility of the thermodynamic limit, another **critical slowing down** (see Section 3.4). The following section will explain the mentioned finite size corrections to static scaling and illustrate how they can be used to analyze critical exponents.

3.3 Finite-size Scaling and Critical Exponent Extraction

The system size L transforms after RG transformation according to

$$R_l(L) = L^{(l)} = L/l \ , \tag{3.30}$$

analogous to the correlation length. Extending the transformation of the free energy density of Equation 3.2 by a dependence of the system size yields

$$f\left([K], L^{-1}\right) = l^{-2} f\left([K^{(l)}], {L^{(l)}}^{-1}\right) = l^{-2} f\left([K^{(l)}], lL^{-1}\right) \ , \tag{3.31}$$

the **finite-size scaling** (FSS) of f. Let $K_1 = \varepsilon$ be the reduced temperature. Close to the critical point Equation 3.24 can be used to write Equation 3.31 in terms of eigenvalues

$$f\left(\varepsilon, K_2, ..., L^{-1}\right) = l^{-2} f\left(\varepsilon l^{y_\varepsilon}, K_2 l^{y_2}, ..., lL^{-1}\right) \ . \tag{3.32}$$

The system size behaves like a relevant coupling constant with an eigenvalue of

$$\lambda_L = 1 \ , \qquad \text{implying that} \qquad y_L = 1 \ . \tag{3.33}$$

This means that the system size has to be tuned to criticality for the phase transition to occur. Like ε, the inverse system size has to be set zero $L^{-1} = 0$ which is equivalent to taking the thermodynamic limit. As a result, real, finite systems deviate from the behavior that scaling laws dictate. The actual correlation length cannot outgrow the system size $\xi_L \leq L$ and so the divergence of ξ is rounded at the phase transition. Additionally, the peak of $\xi_L(T)$ is shifted [25] (to a lower critical temperature?). The ideal behavior of ξ is compared to the behavior of a finite system in Figure 3.2.

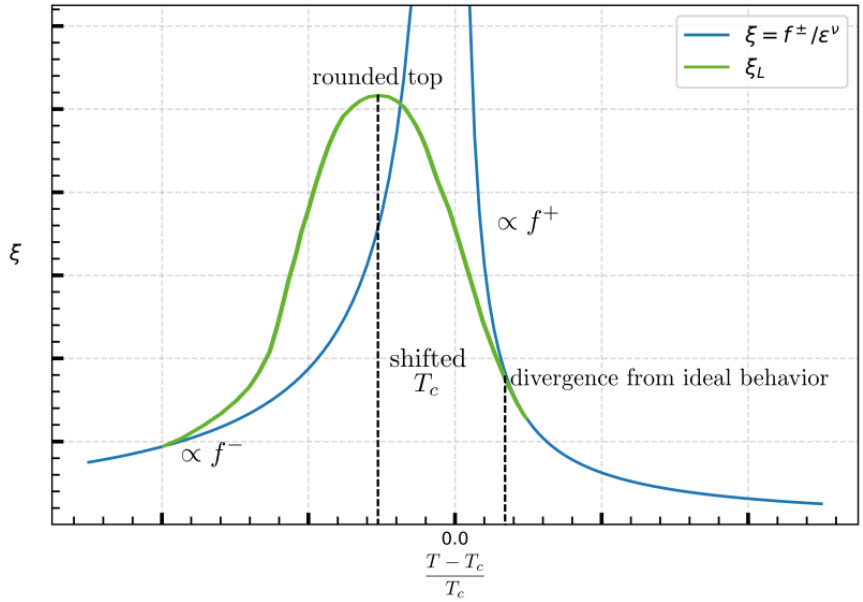

Figure 3.2: The equilibrium correlation length ξ is shown versus the reduced critical temperature. In the thermodynamic limit, ξ diverges at the critical point according to a power law, as depicted by the blue line. For finite systems, the singularity of ξ appears rounded as shown by the green curve. The peak position is shifted to an effective critical temperature.

Now consider Equation 3.26 extended by L-dependence reading

$$\xi(\varepsilon, L^{-1}) = l\xi(\varepsilon l^{y_\varepsilon}, lL^{-1}) = \varepsilon^{-\nu} F_\xi(L^{-1}\varepsilon^{-\nu}) \ , \tag{3.34}$$

with F_ξ as in Equation 3.27. Introducing a new scaling function $F' = (L\varepsilon^\nu)^{-1} F_\xi$ yields

$$\xi(\varepsilon, L^{-1}) = \varepsilon^{-\nu}(L\varepsilon^\nu)F'(L\varepsilon^\nu) = LF'(L\varepsilon^\nu) \ . \tag{3.35}$$

In the limit $L \to \infty$ and close to $\varepsilon = 0$, ξ has to scale like $\xi(\varepsilon, 0) \propto \varepsilon^{-\nu}$ implying that

$$\lim_{L\to\infty} \lim_{\varepsilon\to 0} F'(L\varepsilon^\nu) \propto (L\varepsilon^\nu)^{-1} \ . \tag{3.36}$$

The correlation length is capped for finite L so that at the critical point $\xi(0, L^{-1}) \propto L$. For F' this means

$$\lim_{\varepsilon\to 0} F'(L\varepsilon^\nu) \propto \text{const.} \ , \tag{3.37}$$

showing that the scaling function does not diverge. Therefore a Taylor expansion around $\varepsilon = 0$

is reasonable and gives

$$\frac{L}{\xi(\varepsilon, L^{-1})} = A + B\varepsilon L^{1/\nu} + O(\varepsilon^2) \ . \tag{3.38}$$

This equation is an important result since it can be used to calculate two central quantities. Firstly, curves of $L/\xi(\varepsilon, L^{-1})$ for different L intersect at the critical point $\varepsilon = 0$. Hence, by determining this intersection one can extract the critical temperature T_c, which is usually not known a priori. Secondly by computing the gradient

$$\frac{\partial}{\partial\varepsilon}\left(\frac{L}{\xi(\varepsilon, L^{-1})}\right) = BL^{1/\nu} \tag{3.39}$$

for various L, one can determine the critical exponent ν. This method is easier than, for example, trying to fit to the original scaling law Equation 3.27 because of the reasons mentioned at the end of Section 3.2.

3.3.1 Binder Cumulant

FFS scaling laws like Equation 3.38 can be derived for any thermodynamic quantity [56, 9]. The Binder cumulant U_L, introduced by K. Binder in [7], is frequently used to investigate simulations. It is defined as

$$U_L = \frac{\langle M_L^4 \rangle}{\langle M_L^2 \rangle^2} \ , \tag{3.40}$$

with M_L being the order parameter of a system of size L. The ensemble average $\langle \cdot \rangle$ denotes the mean of infinitely many system realizations. Its finite size scaling is analogous to Equation 3.38 given by

$$U_L = U^* + U\varepsilon L^{1/\nu}\left(1 + WL^{-\omega} + ...\right) \ , \tag{3.41}$$

including corrections resulting out of the largest irrelevant eigenvalue $1/|y_1| = \omega$. To extract the critical exponent ν a linear fit to

$$\ln\left(\frac{\partial U_L}{\partial\varepsilon}\right) \approx \ln\left(UL^{1/\nu}\right) = \ln(U) + \frac{1}{\nu}\ln(L) \ . \tag{3.42}$$

is performed. The Binder cumulant has a value of $U_L = 1$ far below the phase transition, approaches $U_L = 3$ above the phase transition and exhibits the intersection in between at $U_L = U^*$. It is generally easy to compute and extract.

3.4 Dynamic Scaling and the Kibble-Zurek Mechanism

3.4.1 The Relaxation Time τ and the Critical Exponent z

With the Binder cumulant we acquired a way to extract the static scaling exponent ν. Aside static scaling, **dynamic critical phenomena** are of central importance to describe phase transitions. Dynamic scaling describes how much time fluctuations in systems take to equilibrate. This time is called the **relaxation time** τ_k and it is usually specified for different lengthscales with the wavenumber k. The zero wavenumber relaxation time $\tau_0 = \tau$ quantifies relaxation on the largest lengthscales. Its scaling [29]

$$\tau = \tau_\xi \xi(\varepsilon)^z \tag{3.43}$$

defines a new **dynamic critical exponent** z. (TODO RG explanation for this scaling?).

Plugging in the known scaling of $\xi(\varepsilon)$ from Section 3.2 yields

$$\tau = \tau_\xi \xi(\varepsilon)^z = \tau_\xi \left(f^\pm |\varepsilon|^{-\nu}\right)^z := \tau_\varepsilon |\varepsilon|^{-\nu z} \ . \tag{3.44}$$

As the correlation length diverges, so does the relaxation time. Interpreting ξ as a characteristic length at which system components are still influenced by each other gives an intuitive explanation for this divergence. The maximum speed for the propagation of interactions in the system is the respective speed of sound. Even the speed of sound would need an infinite amount of time to cover an infinite distance. In practice the propagation will take much more time. This is the in Section 3.2 mentioned phenomenon of critical slowing down. As a system approaches $\varepsilon \to 0$, it takes longer and longer to equilibrate. It then becomes a computational challenge to let large systems equilibrate. But since static scaling laws describe quantities in equilibrium and are only valid in the thermodynamic limit for $\varepsilon \to 0$, large, critical systems have to be considered. This dilemma was partially solved by the finite size techniques of Section 3.3.

As well as its complementary static phenomenon does the dynamic scaling exhibit universality. The static and dynamic universality classes are not independent, but the dynamic ones form subgroups of the static universality classes. Besides the usual indicators described in Section 3.2, the conservation laws that are fulfilled by the system, as well as Poisson-bracket relations between the order parameter and the conserved densities are decisive for the respective universality class. The important anisotropic Ising model is part of Model A as specified by Hohenberg and Halperin [29]. Its dynamic critical exponent can be expressed in terms of

$$z = 2 + c\eta \ , \tag{3.45}$$

with η as in Table 3.1 and c a constant to be determined.

3.4.2 Quenches and the Freezeout of Domains

Systems like the Si(001) surface that exhibit order-disorder phase transitions usually have multiple possible orderings in the low temperature state. Boundaries between domains of different order, also called domain walls, are stable topological defects. The **Kibble-Zurek mechanism** (KZM) [36, 74, 75] describes the final density of topological defects after driving a system through its phase transition. It directly relates the correlation length to the static and dynamic critical exponents ν and z through a scaling law that has been verified in numerous experiments [64, 71, 60]. The KZM shall be a central point of the upcoming investigations and will be explained in the following.

We will solely consider linear quenches, concretely the cooldown of a system linear in time t. The speed of cooling is characterized by the **quench timescale** τ_Q defined by

$$\varepsilon(t) = \frac{t}{\tau_Q} \ . \tag{3.46}$$

For slow quenches sufficiently far away from the critical point, the system will evolve adiabatically, meaning that thermodynamic quantities like ξ assume their equilibrium values. As the system approaches the phase transition at $t = 0$, the derivative

$$\frac{\partial}{\partial t}\xi(\varepsilon(t)) = -\nu f^{\pm}\frac{(\tau_Q)^{\nu}}{t^{-(\nu+1)}} \tag{3.47}$$

diverges and at some point will eventually outgrow the reaction capability of the system. The actual correlation length will diverge from its equilibrium behavior like shown in Figure 3.3. The timepoint $\hat{t}$ of divergence from the equilibrium behavior is called the **freezeout** since the current state of the system effectively becomes frozen in comparison with the equilibrium values. The KZM states that the freezeout roughly happens at

$$\tau(\hat{t}) = \hat{t} \ , \tag{3.48}$$

so as soon as τ exceeds the time that is left until the critical point is crossed. The system quantities after the quench will be directly related to their equilibrium values at $\hat{t}$. Combining

$$\hat{t} = \varepsilon(\hat{t})\tau_Q \qquad \text{and} \qquad \hat{t} = \tau(\hat{t}) = \tau(\varepsilon(\hat{t})) = \tau_\varepsilon\left|\varepsilon(\hat{t})\right|^{-\nu z} \tag{3.49}$$

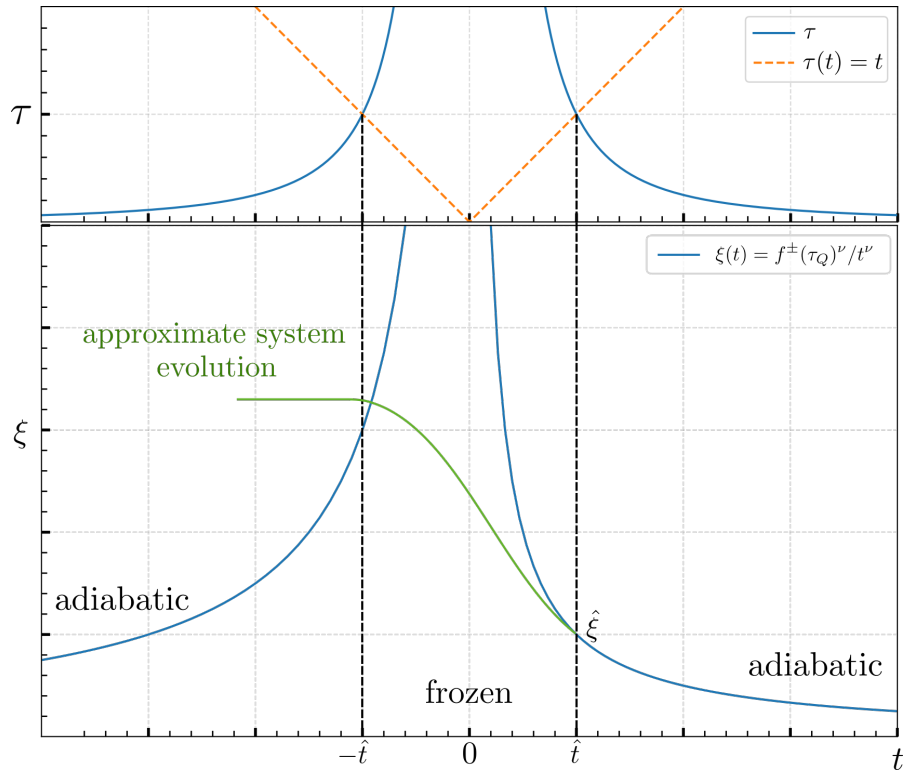

Figure 3.3: In the top plot the divergence of the relaxation time τ, i.e. the critical slowing down, is shown in blue versus the time t during a linear quench. The freezeout of the current state happens roughly at $\tau(\hat{t}) = \hat{t}$, visualized by the intersection with the dotted orange line. In the bottom plot the divergence of the equilibrium ξ on the quench time is shown. Before $\hat{t}$ a quenched system evolves approximately adiabatic, following the blue line. After the freezeout, the actual correlation diverges from the equilibrium behavior, shown by the green line. Note that in this parameterization, a cooling quench runs from $t > 0$ to $t < 0$. The frozen domain walls are topologically stable in time.

yields the reduced temperature at $\hat{t}$

$$\left|\varepsilon(\hat{t})\right| = \left(\frac{\tau_\varepsilon}{\tau_Q}\right)^{\frac{1}{1+\nu z}} . \tag{3.50}$$

For the scaling of ξ this means

$$\xi \propto \hat{\xi} := \xi(\varepsilon(\hat{t})) = \xi_0/|\varepsilon(\hat{t})|^\nu = \xi_0 \left|\frac{\tau_Q}{\tau_\varepsilon}\right|^{\frac{\nu}{1+\nu z}} , \tag{3.51}$$

so the frozen value of the correlation length scales with the quench timescale like $\hat{\xi} \propto \tau_Q^{\frac{\nu}{1+\nu z}}$. The freezeout of the correlation length implies domains of order with an extent proportional $\hat{\xi}^2$. The domain walls separating ordered areas may have influences on different properties of the surface, including conductivity, an important quantity for the semiconductor industry. Knowledge of how the defect density on the surface behaves might help to prepare ideal silicon surfaces.

It is important to note that the KZM is a statistical phenomenon and will only be able to predict how the frozen correlation lengths will behave on average for many quenches or very large systems. In general the freezeout correlation length $\hat{\xi}$ as well as the final correlation length will naturally differ from the predicted behavior, at least locally.

4 Simulating Dynamics

While most numerical studies of phase transitions rely on Monte Carlo techniques [62, 20, 27], this work, inspired by Laguana and Zurek [42], focuses on the use of **stochastic differential equations**. Their mathematical basics and a derivation of a Langevin equation for our case will be outlined in the following.

4.1 Stochastic Differential Equations and the Langevin Equation

4.1.1 Stochastic Differential Equations

Put simply, stochastic differential equations (SDEs) are the stochastic generalizations of common differential equations like

$$y(t + \mathrm{d}t) = y(t) + A(y(t), t)\mathrm{d}t \ , \tag{4.1}$$

with an infinitesimal time interval $\mathrm{d}t$ and a given function $A(y(t), t)$. Equation (4.1) describes a **continuous, memoryless, deterministic** process. For every timepoint $t+\mathrm{d}t$, one can predict the value $y(t + \mathrm{d}t)$ knowing the values $y(t)$ and $\mathrm{d}t$. SDEs describe continuous, memoryless **stochastic** processes, also called continuous **Markov processes**. For every timepoint we can assign definite probabilities to all $y(t + \mathrm{d}t)$. These properties impose strict limitations on a generalization of Equation 4.1. It turns out that the generalization must be of the form [23]

$$y(t + \mathrm{d}t) = y(t) + A(y(t), t)\mathrm{d}t + D^{1/2}\left(y(t), t\right) n(t)(\mathrm{d}t)^{1/2} \ . \tag{4.2}$$

The random number $n(t)$ is a sample value of a normal distribution $\mathcal{N}(0, 1)$ around zero with unit standard deviation. $A(y(t), t)$ and $D(y(t), t)$ are called the **drift** and **diffusion** function. Equation 4.2 is called the standard form **Langevin equation** and it represents an update formula for the continuous Markov process. To obtain the widely used **differential** or **white noise** form of the Langevin equation, we define the **Gaussian white noise process** $\Gamma(t)$ by

$$\Gamma(t) := \lim_{\mathrm{d}t\to 0} \mathcal{N}(0, 1/\mathrm{d}t) \equiv \lim_{\mathrm{d}t\to 0} \frac{n(t)}{(\mathrm{d}t)^{1/2}}. \tag{4.3}$$

Its expectation values $\langle \dot{} \rangle$ satisfy

$$\langle \Gamma(t) \rangle = 0 \qquad \text{and} \qquad \langle \Gamma(t)\Gamma(t+t') \rangle = \delta(t') \ . \tag{4.4}$$

Rearranging Equation 4.2 to

$$\frac{y(t+\mathrm{d}t) - y(t)}{\mathrm{d}t} = A(y(t),t) + D^{1/2}(y(t),t)\frac{n(t)}{(\mathrm{d}t)^{1/2}} \ , \tag{4.5}$$

and taking the limit $\mathrm{d}t \to 0$ yields the differential form

$$\frac{d}{\mathrm{d}t}y(t) = A(y(t),t) + D^{1/2}(y(t),t)\Gamma(t) \ . \tag{4.6}$$

Einstein showed that $A(y(t),t)$ and $D(y(t),t)$ are not independent if they are supposed to accurately describe a thermodynamic system [19]. Their relation will be subject of the next section.

4.1.2 Ornstein-Uhlenbeck Process and Brownian Motion

The Ornstein-Uhlenbeck (OU) process is central to the mathematical description of Brownian motion with linear forces. Put simply, Brownian motion in a potential will be used to model the movement of the silicon dimers. The Ornstein-Uhlenbeck process is a continuous Markov process with drift and diffusion functions of the form

$$A(y(t),t) = -\frac{1}{\zeta}y(t) \qquad \text{and} \qquad D(y(t),t) = c \ . \tag{4.7}$$

The constants ζ and c are the **relaxation time** and the **diffusion constant**. Plugging these functions into Equation 4.2 gives

$$y(t+\mathrm{d}t) = y(t) - \frac{1}{\zeta}y(t)\mathrm{d}t + c^{1/2}n(t)(\mathrm{d}t)^{1/2} \ . \tag{4.8}$$

The quantity $y(\mathrm{d}t)$ is normally distributed since it is the sum of a constant $y(0)$ and the normal random variable $n(\mathrm{d}t)$. Hence, $y(2dt)$ is normally distributed, being the linear combination of two statistically independent normal random variables $y(\mathrm{d}t)$ and $n(2dt)$. By induction $y(t)$ is normally distributed for all times. Calculating mean and variance of $y(t)$ determines its distribution. The differential equations for the first and second moment of y are

$$\langle y(t+\mathrm{d}t) \rangle = \langle y(t) \rangle - \frac{1}{\zeta}\langle y(t) \rangle \mathrm{d}t \ , \tag{4.9}$$

and

$$\left\langle y^2(t+\mathrm{d}t)\right\rangle = \left\langle y^2(t)\right\rangle - \frac{2}{\zeta}\left\langle y^2(t)\right\rangle \mathrm{d}t + c\ \mathrm{d}t\ . \tag{4.10}$$

Solving them with the initial condition $y(0) = y_0$ yields the mean

$$\langle y(t)\rangle = y_0 e^{-t/\zeta} \tag{4.11}$$

and the variance

$$\left\langle y^2(t)\right\rangle - \langle y(t)\rangle^2 = \frac{c\zeta}{2}\left(1 - e^{-2t/\zeta)}\right) \tag{4.12}$$

of $y(t)$. This determines the distribution of $y(t)$ to be

$$y(t) = \mathcal{N}\left(y_0 e^{-t/\zeta}, \frac{c\zeta}{2}\left(1 - e^{-2t/\zeta)}\right)\right) \overset{t\to\infty}{=} \mathcal{N}\left(0, \frac{c\zeta}{2}\right)\ . \tag{4.13}$$

Now consider a particle with mass m and momentum p that is coupled to a reservoir of temperature T. The interaction with the bath results in a dissipative drag force $-(\eta/m)p(t)$ proportional to a dampening constant η as well as a fluctuating force $F(t)$. By Newton's second law, its equation of motion is given by

$$\frac{\mathrm{d}}{\mathrm{dt}}p(t) = -\frac{\eta}{m}p(t) + F(t). \tag{4.14}$$

This equation is identified with Equation 4.8 with $y(t) = p(t)$

$$\frac{\mathrm{d}}{\mathrm{dt}}p(t) = -\frac{1}{\zeta}p(t) + c^{1/2}\Gamma(t). \tag{4.15}$$

According to Maxwell-Boltzmann statistics, the directional velocity of the particles will be normally distributed around $\mu_v = 0$ with a standard deviation of $\sigma_v^2 = k_B T/m$. Normal distributions satisfy

$$a + b\mathcal{N}(\mu, \sigma^2) = \mathcal{N}(a + b\mu, b^2\sigma^2)\ , \tag{4.16}$$

so for the momentum distribution

$$p(t \to \infty) = \mathcal{N}(0, mk_B T) \tag{4.17}$$

follows. Comparing Equations 4.13 and 4.17 shows that

$$\frac{c\zeta}{2} = mk_B T\ , \qquad \text{or equivalently} \qquad c = 2k_B T\eta\ . \tag{4.18}$$

Hence, the fluctuating force $F(t)$ can be rewritten as

$$F(t) = \sqrt{2k_B T\eta}\Gamma(t) \ , \tag{4.19}$$

confirming that drift and diffusion are not independent. This is a simple form of the powerful **fluctuation-dissipation theorem**.

For a particle **in a potential** $V(x)$ one eventually obtains the equations of motions

$$\frac{\mathrm{d}}{\mathrm{dt}}x(t) = \frac{1}{m}p(t) \qquad \text{and} \tag{4.20}$$

$$\frac{\mathrm{d}}{\mathrm{dt}}p(t) = -\frac{\eta}{m}p(t) - \frac{\partial V(x)}{\partial x} + \sqrt{2k_B T\eta}\Gamma(t) \ . \tag{4.21}$$

Methods of numerical solution of the Langevin equation will be presented in Section 4.3. But first the applicability of the Langevin equation for the silicon surface will be verified.

4.2 Quantum Mechanical Considerations

4.2.1 Caldeira-Leggett Master Equation

The silicon surface is a complex system subject to quantum mechanical interactions between the surface atoms, as well as with the bulk. The bulks is much larger than the surface and acts as a thermal reservoir, interacting with the dimers through lattice excitations. It is not obvious that classical Langevin equations will be valid in this case. Systems that are coupled to an environment are subject of the theory of open quantum systems, which will be used to derive a set of coupled Langevin equations.

Consider the **Caldeira-Leggett model** [13] for a quantum mechanical particle of mass m, moving in a potential $V(\hat{x})$. We can write its **free Hamiltonian** $\hat{H}_S$ as

$$\hat{H}_S = \frac{1}{2m}\hat{p}^2 + V(\hat{x}) \ , \tag{4.22}$$

with the position and momentum operators $\hat{x}$ and $\hat{p}$. The reservoir, which is the silicon bulk, is modeled as a set of harmonic oscillators with frequencies ω_n. The bath Hamiltonian $\hat{H}_B$ can be written in terms of the bosonic annihilation and creation operators $\hat{b}_n^\dagger$ and $\hat{b}_n$, or in terms of the canonically conjugated position $\hat{x}_n$ and momentum $\hat{p}_n$ operators

$$\hat{H}_B = \sum_n \hbar\omega_n \left(\hat{b}_n^\dagger \hat{b}_n + \frac{1}{2}\right) = \sum_n \left(\frac{1}{2m_n}\hat{p}_n^2 + \frac{1}{2}m_n\omega_n^2\hat{x}_n^2\right) \ . \tag{4.23}$$

We assume that $\hat{x}$ is linearly coupled to the $\hat{x}_n$, yielding the interaction Hamiltonian $\hat{H}_I$

$$\hat{H}_I = -\hat{x} \otimes \sum_n \kappa_n \hat{x}_n = -\hat{x} \otimes \sum_n \kappa_n \sqrt{\frac{\hbar}{2m_n\omega_n}} \left(\hat{b}_n + \hat{b}_n^\dagger\right) =: -\hat{x} \otimes \hat{B} \ , \tag{4.24}$$

with the coupling constants κ_n. The Hamiltonian of the combined system is given by

$$\hat{H}_{SB} = \hat{H}_S + \hat{H}_B + \hat{H}_I \ . \tag{4.25}$$

The combined system is visualized for the case of the Si(001) surface in Figure 4.1. To guarantee positivity of the $\hat{H}_{SB}$, a **counter-term**

$$\hat{H}_c = \hat{x}^2 \sum_n \frac{\kappa_n^2}{2m_n\omega_n^2} \tag{4.26}$$

is added. Positive Hamiltonians have solely positive eigenvalues, ensuring that the physical frequencies of motion of the Brownian particle are reproduced. In the following the counter-term is absorbed into $\hat{H}_S$.

Since it is neither possible, nor required to solve the dynamics of the whole Hamiltonian, a probabilistic description will be developed. In quantum mechanics this is achieved by modeling the system density matrix $\hat{\rho}_S$. The density matrix of the composite system in **interaction picture** with respect to $\hat{H}_S + \hat{H}_B$ is given by

$$\hat{\boldsymbol{\rho}}_{SB} := e^{\mathrm{i}\left(\hat{H}_S+\hat{H}_B\right)t} \hat{\rho}_{SB} e^{-\mathrm{i}\left(\hat{H}_S+\hat{H}_B\right)t} \ . \tag{4.27}$$

Operators in interaction picture are printed **bold** in the following. The time evolution of $\hat{\boldsymbol{\rho}}_{SB}$ is

$$\frac{\partial}{\partial t}\hat{\boldsymbol{\rho}}_{SB}(t) = -\mathrm{i}\left[\hat{\boldsymbol{H}}_I(t), \hat{\boldsymbol{\rho}}_{SB}(t)\right] \ . \tag{4.28}$$

To derive an equation for $\hat{\boldsymbol{\rho}}_S$ the reservoir degrees of freedom are traced out

$$\begin{aligned}
\frac{\partial}{\partial t}\hat{\boldsymbol{\rho}}_S(t) &= \mathrm{tr}_B\left\{\frac{\partial}{\partial t}\hat{\boldsymbol{\rho}}_{SB}(t)\right\} = -\mathrm{i}\ \mathrm{tr}_B\left\{\left[\hat{\boldsymbol{H}}_I(t), \hat{\boldsymbol{\rho}}_{SB}(t)\right]\right\} \\
&= -\mathrm{i}\ \mathrm{tr}_B\left\{\left[\hat{\boldsymbol{H}}_I(t), \hat{\boldsymbol{\rho}}_{SB}(0)\right]\right\} - \int_0^t \mathrm{d}t'\ \mathrm{tr}_B\left\{\left[\hat{\boldsymbol{H}}_I(t), \left[\hat{\boldsymbol{H}}_I(t'), \hat{\boldsymbol{\rho}}_{SB}(t')\right]\right]\right\} \\
&= -\int_0^t \mathrm{d}t'\ \mathrm{tr}_B\left\{\left[\hat{\boldsymbol{H}}_I(t), \left[\hat{\boldsymbol{H}}_I(t'), \hat{\boldsymbol{\rho}}_S(t') \otimes \overline{\rho}_B\right]\right]\right\} \ .
\end{aligned} \tag{4.29}$$

The second line in Equation 4.29 is obtained by integrating Equation 4.28 and solving for $\hat{\boldsymbol{\rho}}_{SB}(0)$. The **Born approximation** assumes that the reservoir density matrix is stationary.

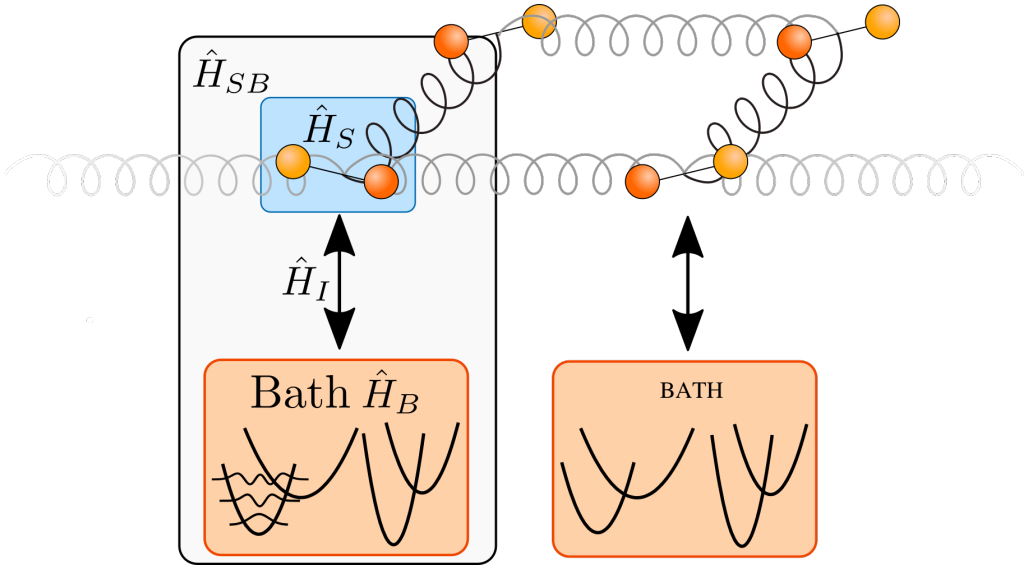

Figure 4.1: (CONCEPT) In the theory of open quantum systems, a system that is thermally coupled to an environment is modeled by a composite Hamiltonian $\hat{H}_{SB} = \hat{H}_S + \hat{H}_B + \hat{H}_I$. $\hat{H}_S$ denotes the system Hamiltonian describing the potential acting on the dimer. The reservoir is modeled as a set of harmonic oscillators captured in $\hat{H}_B$. The interaction between a dimer and the bath are contained in $\hat{H}_I$. We approximate that every dimer is coupled to a separate bath.

In this case, the composite density matrix decomposes to $\hat{\boldsymbol{\rho}}_{SB}(t) = \hat{\boldsymbol{\rho}}_S(t) \otimes \overline{\rho}_B$ and the trace

$$\mathrm{tr}_B \left\{ \left[\hat{\boldsymbol{H}}_I(t), \hat{\boldsymbol{\rho}}_{SB}(0) \right] \right\} = 0 \tag{4.30}$$

vanishes. The integrand in Equation 4.29 typically decays rather fast. Hence, the **Markov approximation** [44] is applicable. This involves the replacement $\hat{\boldsymbol{\rho}}_S(t') \to \hat{\boldsymbol{\rho}}_S(t)$, as well as sending the upper limit of the integral to infinity. Substituting $\tau = t - t'$ yields the **Redfield-II** master equation

$$\frac{\partial}{\partial t}\hat{\boldsymbol{\rho}}_S(t) = -\int_0^\infty \mathrm{d}\tau \ \mathrm{tr}_B \left\{ \left[\hat{\boldsymbol{H}}_I(t), \left[\hat{\boldsymbol{H}}_I(t-\tau), \hat{\boldsymbol{\rho}}_S(t) \otimes \overline{\rho}_B \right] \right] \right\} \ . \tag{4.31}$$

Transforming Equation 4.31 back to the Schrödinger picture gives

$$\frac{\partial}{\partial t}\hat{\rho}_S(t) = -\mathrm{i} \ \left[\hat{H}_S, \rho_S(t) \right] - \int_0^\infty \mathrm{d}\tau \ \mathrm{tr}_B \left\{ \left[\hat{H}_I, \left[\hat{\boldsymbol{H}}_I(-\tau), \hat{\rho}_S(t) \otimes \overline{\rho}_B \right] \right] \right\} \ . \tag{4.32}$$

The integral in the second term of Equation 4.32 can be rearranged to

$$\int_0^\infty \mathrm{d}\tau \left(\frac{\mathrm{i}}{2} D(\tau) \left[\hat{x}, \{ \hat{\boldsymbol{x}}(-\tau) . \hat{\rho}_S(t) \} \right] - \frac{1}{2} D_1(\tau) \left[\hat{x}, [\hat{\boldsymbol{x}}(-\tau), \hat{\rho}_S(t)] \right] \right) \ , \tag{4.33}$$

with the noise kernel $D_1(\tau)$ and dissipation kernel $D(\tau)$ defined as in Section A.1. The noise and dissipation kernels disappear on the timescale of the relaxation τ_B of the reservoir. When

doing the Markov approximation it is assumed that this timescale is much shorter than the relaxation time of the system τ_S. This is used again by approximating $\hat{\boldsymbol{x}}(-\tau)$ by its free dynamics

$$\hat{\boldsymbol{x}}(-\tau) = \hat{x} - \hat{p}\tau \ . \tag{4.34}$$

Plugging this approximation into Equation 4.33 allows for the evaluation of the integrals (see Section A.1). This eventually yields the **Caldeira-Leggett master equation**

$$\frac{\mathrm{d}}{\mathrm{d}t}\rho_S(t) = \underbrace{-\mathrm{i}\left[\hat{H}_S, \rho_S(t)\right]}_{\text{free dynamics}} \underbrace{-\mathrm{i}\eta\Big[\hat{x}, \{\hat{p}, \rho_S(t)\}\Big]}_{\text{dissipative term}} \underbrace{-2\eta m k_B T\Big[\hat{x}, \big[\hat{x}, \rho_S(t)\big]\Big]}_{\text{thermal fluctuations}} \ . \tag{4.35}$$

The damping constant η enters the calculation through a parametrization of the spectral density function of the reservoir. The first term in the Caldeira-Leggett master equation describes the free dynamics of the system and resembles the form of the **von-Neumann** equation. The second term is the dissipative part proportional to the damping constant η. The thermal fluctuations of the reservoir are captured in the third term proportional to the temperature T. The state of the reservoir $\overline{\rho}_B$ follows the **Bose-Einstein distribution** and determines T.

4.2.2 Equations of Motion

From Equation 4.35 one can derive equations of motion for arbitrary observables via

$$\frac{\mathrm{d}}{\mathrm{d}t}\left\langle \hat{A} \right\rangle = \mathrm{tr}\left\{ \hat{A}\frac{\mathrm{d}}{\mathrm{d}t}\hat{\rho}_S(t) \right\} \ . \tag{4.36}$$

Version 1: Comparing the results of Equation 4.36 for $\hat{x}, \hat{p}$ and $\hat{p}^2$ to the equations of Brownian motion of subsection 4.1.2

$$\begin{aligned}
\frac{\mathrm{d}}{\mathrm{d}t}\langle \hat{x} \rangle &= \frac{1}{m}\langle \hat{p} \rangle \ , \\
\frac{\mathrm{d}}{\mathrm{d}t}\langle \hat{p} \rangle &= -\left\langle \frac{\partial V(\hat{x})}{\partial \hat{x}} \right\rangle - \eta \langle \hat{p} \rangle \ , \\
\frac{\mathrm{d}}{\mathrm{d}t}\langle \hat{p}^2 \rangle &= -\left\langle \hat{p}\frac{\partial V(\hat{x})}{\partial \hat{x}} + \frac{\partial V(\hat{x})}{\partial \hat{x}}\hat{p} \right\rangle \\
&\quad - 2\eta \langle \hat{p}^2 \rangle + 2\eta k_B T \ ,
\end{aligned}
\qquad
\begin{aligned}
\frac{\mathrm{d}}{\mathrm{d}t}\langle x(t) \rangle &= \frac{1}{m}\langle p(t) \rangle \ , \\
\frac{\mathrm{d}}{\mathrm{d}t}\langle p(t) \rangle &= -\left\langle \frac{\partial V(x)}{\partial x} \right\rangle - \eta \langle p(t) \rangle \ , \\
\frac{\mathrm{d}}{\mathrm{d}t}\langle p^2(t) \rangle &= -\left\langle 2p(t)\frac{\partial V(x)}{\partial x} \right\rangle \\
&\quad - 2\eta \langle p^2(t) \rangle + 2\eta k_B T \ .
\end{aligned}$$

shows that the two equation sets share the same structure.

Version 2:

The results of Equation 4.36 for $\hat{x}, \hat{p}$ and $\hat{p}^2$ are compared to the equations of Brownian motion

Table 4.1: Version2.1.The equations of motion for $\hat{x}, \hat{p}$ and $\hat{p}^2$ calculated from Equation 4.36 are compared to Brownian motion of subsection 4.1.2. It is evident that the structure of equations of motion for the quantum expectation values matches the expectation values from Brownian motion. Therefore the quantum mechanical case is called **Quantum Brownian Motion**.

Quantum Brownian Motion	
Eq. for $\langle\hat{x}\rangle$:	$\frac{\mathrm{d}}{\mathrm{d}t}\langle\hat{x}\rangle = \frac{1}{m}\langle\hat{p}\rangle$
Eq. for $\langle\hat{p}\rangle$:	$\frac{\mathrm{d}}{\mathrm{d}t}\langle\hat{p}\rangle = -\left\langle\frac{\partial V(\hat{x})}{\partial\hat{x}}\right\rangle - \eta\langle\hat{p}\rangle$
Eq. for $\langle\hat{p}^2\rangle$:	$\frac{\mathrm{d}}{\mathrm{d}t}\langle\hat{p}^2\rangle = -\left\langle\hat{p}\frac{\partial V(\hat{x})}{\partial\hat{x}} + \frac{\partial V(\hat{x})}{\partial\hat{x}}\hat{p}\right\rangle - 2\eta\langle\hat{p}^2\rangle + 2\eta k_B T$
Brownian Motion	
Eq. for $\langle x(t)\rangle$:	$\frac{\mathrm{d}}{\mathrm{d}t}\langle x(t)\rangle = \frac{1}{m}\langle p(t)\rangle$
Eq. for $\langle p(t)\rangle$:	$\frac{\mathrm{d}}{\mathrm{d}t}\langle p(t)\rangle = -\left\langle\frac{\partial V(x)}{\partial x}\right\rangle - \eta\langle p(t)\rangle$
Eq. for $\langle p^2(t)\rangle$:	$\frac{\mathrm{d}}{\mathrm{d}t}\langle p^2(t)\rangle = -\left\langle 2p(t)\frac{\partial V(x)}{\partial x}\right\rangle - 2\eta\langle p^2(t)\rangle + 2\eta k_B T$

Table 4.2: Version2.2. The equations of motion for $\hat{x}, \hat{p}$ and $\hat{p}^2$ calculated from Equation 4.36 are compared to Brownian motion of subsection 4.1.2. It is evident that the structure of equations of motion for the quantum expectation values matches the expectation values from Brownian motion. Therefore the quantum mechanical case is called **Quantum Brownian Motion**.

Quantity	Quantum Brownian Motion	Brownian Motion
x	$\frac{\mathrm{d}}{\mathrm{d}t}\langle\hat{x}\rangle = \frac{1}{m}\langle\hat{p}\rangle$	$\frac{\mathrm{d}}{\mathrm{d}t}\langle x(t)\rangle = \frac{1}{m}\langle p(t)\rangle$
p	$\frac{\mathrm{d}}{\mathrm{d}t}\langle\hat{p}\rangle = -\left\langle\frac{\partial V(\hat{x})}{\partial\hat{x}}\right\rangle - \eta\langle\hat{p}\rangle$	$\frac{\mathrm{d}}{\mathrm{d}t}\langle p(t)\rangle = -\left\langle\frac{\partial V(x)}{\partial x}\right\rangle - \eta\langle p(t)\rangle$
p^2	$\frac{\mathrm{d}}{\mathrm{d}t}\langle\hat{p}^2\rangle = -\left\langle\hat{p}\frac{\partial V(\hat{x})}{\partial\hat{x}} + \frac{\partial V(\hat{x})}{\partial\hat{x}}\hat{p}\right\rangle - 2\eta\langle p^2(t)\rangle + 2\eta k_B T$	$\frac{\mathrm{d}}{\mathrm{d}t}\langle p^2(t)\rangle = -\left\langle 2p(t)\frac{\partial V(x)}{\partial x}\right\rangle - 2\eta\langle p^2(t)\rangle + 2\eta k_B T$

of subsection 4.1.2 in Table A.1. The two equation sets share the same structure.

Especially interesting is the last term in the equations for $\langle\hat{p}^2\rangle$. This is the diffusion constant in the case of Brownian motion and it matches the quantum mechanical term. Hence, it is possible to derive the diffusion constant from microscopic considerations. We conclude that the classical equations of motion Equation 4.20 and Equation 4.21 are the classical correspondence to the equations of $\langle\hat{x}\rangle$ and $\langle\hat{p}\rangle$. In the following, the classical equations of motion will be used to describe the silicon surface. Since the silicon dimers interact, the potential $V(x) = V(x, x_i)$ is a function of the coordinates x_i of the other dimers, leading to a **coupling** between the differential equations. Additionally, $V(x, x_i)$ is **nonlinear** in x, eventually yielding a coupled set of nonlinear stochastic differential equations. An analytic solution is impossible

and therefore we turn to numerical solutions in the next section.

4.3 Numerical Methods and Molecular Dynamics

The update-form Equation 4.2 of the Langevin equation is very useful for its numerical solution. A simple method of solution is the straight implementation of Equation 4.2, which is called the **Euler-Maruyama method** [37]. Practically, a system of first-order stochastic differential equations

$$x(t+\mathrm{d}t) = x(t) + \frac{1}{m}p(t)\mathrm{d}t \ , \tag{4.37}$$

$$p(t+\mathrm{d}t) = p(t) - \frac{\eta}{m}p(t)\mathrm{d}t - \frac{\partial V(x(t))}{\partial x}\mathrm{d}t + \sqrt{2k_BT\eta}\ n(t)\sqrt{\mathrm{d}t} \ , \tag{4.38}$$

is solved. The Euler-Maruyama method is straightforward to implement and computationally inexpensive, but shows discretization artefacts even for small stepsizes $\mathrm{d}t$. Since the integration of the equations of motion usually takes much less time than the evaluation of $V(x(t))$ [21], many efforts have been made to improve the weak convergence [37] of integration schemes.

The topic of simulating microscopical systems by numerically solving Newton's equations of motion is called **molecular dynamics**. Molecular dynamics is widely used in biophysics, chemical physics but also material sciences. Larini et al. [45] compare some of the integration schemes that have been developed. They show that the popular Brunger-Brooks-Karplus (BBK) [12] scheme is robust method with a number of general advantages. It integrates in three steps [32], half a kick

$$p\left(t+\tfrac{1}{2}\mathrm{d}t\right) = \left(1-\tfrac{1}{2}\eta\mathrm{d}t\right)p(t) - \tfrac{1}{2}\mathrm{d}t\tfrac{\partial V(x(t))}{\partial x} + \tfrac{1}{2}\sqrt{2\eta k_BT}n(t)\sqrt{\mathrm{d}t} \ , \tag{4.39}$$

drift

$$x(t+\mathrm{d}t) = x(t) + p\left(t+\tfrac{1}{2}\mathrm{d}t\right)\mathrm{d}t \ , \tag{4.40}$$

and half a kick

$$p\left(t\right) = \left(1+\tfrac{\mathrm{d}t}{2}\eta\right)^{-1}\left(p\left(t+\tfrac{\mathrm{d}t}{2}\right) - \tfrac{1}{2}\mathrm{d}t\tfrac{\partial V(x(t+\mathrm{d}t))}{\partial x} + \tfrac{1}{2}\sqrt{2\eta k_BT}n(t+\mathrm{d}t)\sqrt{\mathrm{d}t}\right) \ . \tag{4.41}$$

Compared to higher-order schemes, like the fourth-order Hamiltonian Runge-Kutta scheme [59], that require multiple potential evaluations, the BBK method is faster with limited loss of accuracy [45]. The BBK integration step is slightly slower than the Euler-Maruyama one but it makes up through its much greater stability regarding larger step sizes. This ultimately results in significantly faster simulation speeds. The stability of the schemes is compared in

Section 5.2.

The theoretical foundation for the simulation of the Si(001) surface using Langevin equations is now established. The following section will deal with the modeling of the several times mentioned potential.

4.4 The Model

4.4.1 The Ising model

The Ising model is well known and has been used several times [10, 57, 30, 65] to study the Si(001) surface. Brand et al. [11] found good agreement between the Si(001) phase transition and the Ising critical exponents. Their results are relevant for the following investigations and therefore the Ising model will be shortly discussed below.

The two-dimensional Ising model describes spins $\sigma_{i,j} = \pm 1$ on a lattice. Consider the anisotropic case on a rectangle without external field. Its nearest-neighbor Hamiltonian is given by

$$H = -\sum_{i,j} \left(J_{\parallel} \sigma_{i,j} \sigma_{i,j+1} + J_{\perp} \sigma_{i,j} \sigma_{i+1,j} \right) \ , \tag{4.42}$$

with J_δ, $\delta \in \{\parallel, \perp\}$, being the effective nearest-neighbor coupling strengths. The two-dimensional anisotropic Ising model is analytically solvable [55] and exhibits a continuous phase transition at

$$\sinh\left(\frac{2|J_{\parallel}|}{k_B T_c}\right) \sinh\left(\frac{2|J_{\perp}|}{k_B T_c}\right) = 1. \tag{4.43}$$

The equilibrium correlation lengths for $T > T_c$ can be determined from the coupling constants [50] by

$$\frac{\xi_\delta(T_c)}{a_\delta} = \left(\ln\left[\coth\left(\frac{|J_\delta|}{k_B T_c} \right) \right] - \frac{2|J_{\overline{\delta}}|}{k_B T} \right)^{-1} \ , \tag{4.44}$$

with a_δ being the lattice spacing in δ direction and $\overline{\delta}$ marking the direction perpendicular to δ.

To describe the silicon surface with the Ising model, the equilibrium positions of the silicon dimers in Figure 2.2 (b) are mapped to the Ising spin values $\sigma_{i,j} = \pm 1$. In theoretical works, density functional theory (DFT) calculations are often employed to calculate configuration energies. Equation 4.42 can then be used to fit effective J_δ to the DFT results.

In experiments, the correlation lengths ξ_δ can be measured and used to extract J_δ through Equation 4.44. Calculating quantitative values for J_δ can reveal important information about the nature of the microscopic interactions (between the dimers), especially if Equation 4.42 is extended to next-nearest neighbor couplings or even further. Additionally, theoretical results of the Ising model can be used to analyze the surface further. For example, Equation 4.43 may be used to estimate the transition temperature. Eventually, a simple theoretical model of the Si(001) system is obtained which also may be used in computer simulations.

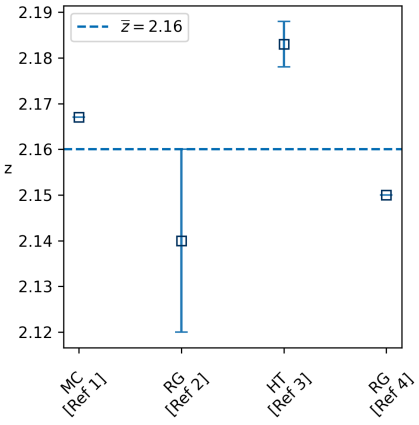

Figure 4.2: Recent results for the dynamic critical exponent z are summarized. The datapoints are obtained by Monte-Carlo methods (MC) [53], renormalization group calculations (RG) [1, 18] and high-temperature expansion (HT) [17].

The Ising model gives name to its universality class. It is characterized by a continuous phase transition with a scalar order parameter and $\mathbb{Z}_2$ symmetry. The static critical exponents of the Ising universality class can be calculated analytically [14]. For ν the exact value

$$\nu = 1 \tag{4.45}$$

is obtained. As noted in Section 3.4, the anisotropic Ising model is part of Model A of critical dynamics [29]. The constant c of Equation 3.45 has been estimated by numerous method. Some recent results for z are shown in Figure 4.2.

Since the Ising model has discrete states, it is not suitable for continuous modeling with equations of motion.

4.4.2 The Classical XY Model

The classical XY model and the Ising model can be viewed as two special cases of the Potts model [58]. It generalizes the Ising model to allow q, instead of two, states. The states are uniformly distributed on a circle as shown in Figure 4.3 (a). In the limit $q \to \infty$ the XY model is obtained. It allows continuous states on the unit circle and is thus suitable to be described by Langevin equations.

The two-dimensional XY Hamiltonian with nearest-neighbor interactions is given by

$$\begin{aligned} H &= -\sum_{i,j} \left(J_{\parallel} \vec{s}_{i,j} \vec{s}_{i,j+1} + J_{\perp} \vec{s}_{i,j} \vec{s}_{i+1,j} \right) \\ &= -\sum_{i,j} \left(J_{\parallel} \cos\left(\vartheta_{i,j} - \vartheta_{i,j+1}\right) + J_{\perp} \cos\left(\vartheta_{i,j} - \vartheta_{i+1,j}\right) \right) \ , \end{aligned} \tag{4.46}$$

with unit-length vectors

$$\vec{s}_{i,j} = \begin{pmatrix} \cos\vartheta_{i,j} \\ \sin\vartheta_{i,j} \end{pmatrix} \ , \tag{4.47}$$

characterizing the state of the lattice site. These rotors are defined by a continuous angle ϑ on the interval $[0, 2\pi)$. Although the exact solution of the two-dimensional XY model is intractable, Mattis [49] used a transfer matrix approach to approximate an analogue to Equation 4.43. He arrived at

$$\frac{2k_B T_c}{J_{\parallel}} \ln\left(\frac{2k_B T_c}{J_{\perp}}\right) = 1 \ , \tag{4.48}$$

with $J_{\parallel} \geq J_{\perp}$. The relation between the coupling constants and the equilibrium correlation lengths is not known at the moment.

The two-dimensional XY model does not exhibit a phase transition in the conventional sense. The **Mermin-Wagner theorem** [51] prohibits the breaking of its continuous O(2) symmetry through short-range interactions. Instead, the system shows the **Kosterlitz-Thouless transition** (KT transition) [38, 6]. The usual power laws are not applicable to this transition because the correlation length diverges exponentially at the critical point. Hence, the two-dimensional XY model does not belong to any universality class.

We can add a p-fold symmetry breaking field of strength h to the XY Hamiltonian

$$H = -\sum_{i,j} \left(J_{\parallel} \cos\left(\vartheta_{i,j} - \vartheta_{i,j+1}\right) + J_{\perp} \cos\left(\vartheta_{i,j} - \vartheta_{i+1,j}\right) \right) + h \sum_{i,j} \cos(p\vartheta_{i,j}) \ , \tag{4.49}$$

explicitly breaking the O(2) symmetry. Such fields may very well be experimentally realized by crystalline anisotropies. The Migdal lattice recursion scheme [52] implies that for $T \to 0$, the field h is a relevant variable in the sense of Section 3.1. The perturbations caused by h will grow as T shrinks, eventually forcing the system into a state of broken symmetry in which one of the directions $\vartheta = 2\pi n/p, n \in [0, p-1]$ is preferred. Hence, any h will lead to deviations in critical behavior from the KT transition. José and Kadanoff [34] found that this

symmetry broken XY model exhibits a continuous phase transition with the critical exponents of a p-state Potts model. This results in Ising critical behavior in the case of $p = 2$. This makes the two-dimensional XY model with twofold symmetry breaking field ideal to explore the dynamics of the Si(001) surface.

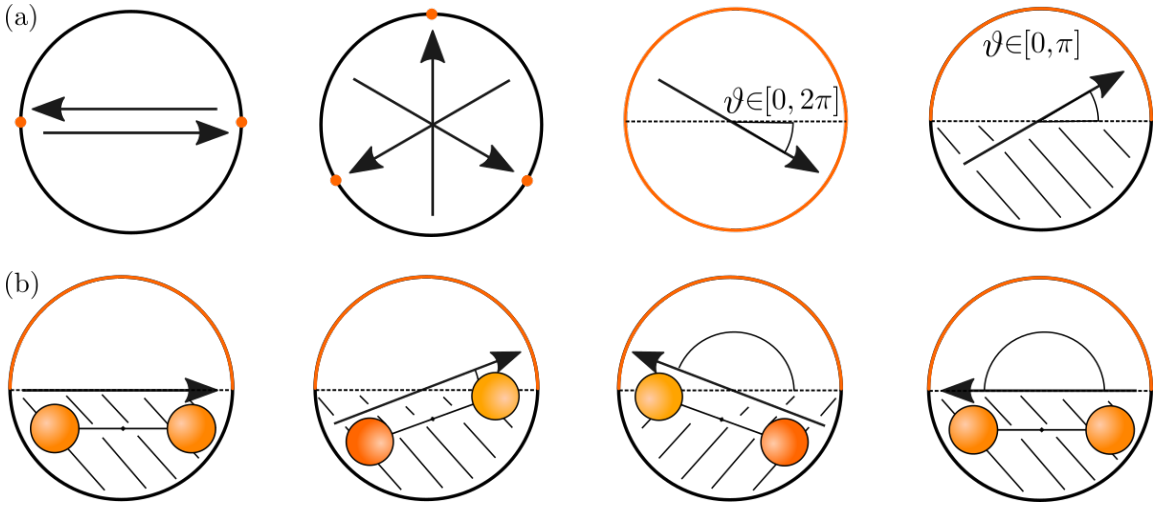

Figure 4.3: Unit circles are shown as visualizations of the state space. The orange parts are the allowed states. The states are depicted as arrows inside the unit circle. **(a)** shows the q-state Potts model. From left to right: The two-state Potts model, or the Ising model, allows only two points on the unit circle. The three-state Potts model allows three different spin directions, visualized by the arrows. In the limit $q \to \infty$ the XY model is obtained. The state is characterized by a continuous angle ϑ. The rightmost circle visualized the adaptation of the XY model to the silicon surface. Here, only half the circle is allowed. **(b)** The buckling angles of the silicon dimers are mapped to the rotors of the XY model. Since the silicon atoms are indistinguishable, a rotation by π maps to the same state. Hence, the state space is only half the unit circle. Note that the left and right vectors are the same state and strictly speaking one of them can be excluded by defining $\vartheta \in [0, \pi)$.

4.4.3 Adaptation to the Si(001) Surface

In the following the XY model will be adapted to optimally resemble the silicon surface.

Like done with the Ising model, the aim is to map the position of the dimer to a model state. The natural choice is to identify the dimer buckling angle with the rotor angle ϑ of the XY model. Since the silicon atoms are indistinguishable, a rotation by π translates into the same state. Hence, only $\vartheta \in [0, \pi)$ define unique states, restricting the state space of the XY model. The resulting half circle is shown in the rightmost picture of Figure 4.3 (a). For computational reasons, ϑ will be shifted by $-\frac{\pi}{2}$, eventually yielding $\vartheta \in \left[-\frac{\pi}{2}, \frac{\pi}{2}\right)$. The restriction is achieved by adding a factor $m = 2$ into the interaction terms

$$J_\delta \cos\left(m \Delta \vartheta_{i,j}\right) \ . \tag{4.50}$$

The equilibrium position of the dimers is majorly influenced by the location of the minima of the symmetry breaking field. The experimental systems shows two stable buckling angles of about $\pm 20°$. Therefore the symmetry breaking field will be constructed to have two minima on the interval $\left[-\frac{\pi}{2}, \frac{\pi}{2}\right)$ at the desired angles. The minima satisfy

$$\cos\left(p\vartheta^{\pm}\right) = -1 \ , \tag{4.51}$$

implying that roughly $p \approx 2.5$. The final resting position of the dimer is shifted by the repulsive interaction of the dimers. This is covered in subsection 5.3.4. The movement of the dimers can be approximated to take place in a double well potential [16]. This is realized by the symmetry breaking shown in Figure 4.4. The question arises if the system still belongs to the Ising universality class if p is a rational number and the allowed states are restricted. This will be subject of subsection 5.3.1.

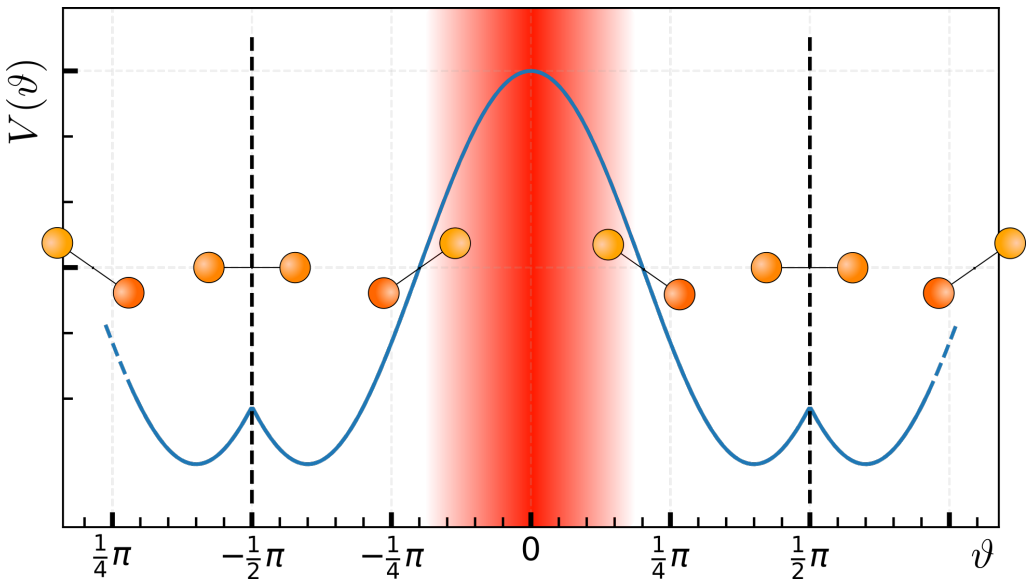

Figure 4.4: The symmetry breaking field h is shown in blue on the dimer angle. The dimer states are defined on $\vartheta \in [-\frac{\pi}{2}, \frac{\pi}{2}]$, therefore h repeats after a period of π. The location of the potential minima are chosen to be located at the according position of the experimental dimers. The red area around $\vartheta = 0$, corresponding to vertical dimers, is strongly suppressed and rarely realized. The dynamics take place in the double well potential shown on the left and on the right of the plot. Some dimer states are depicted at their according angle.

A suitable order parameter for this model is

$$M_L = \frac{1}{L^2} \sum_{i,j} m(\vartheta_{i,j}) \qquad \text{with} \qquad m(\vartheta) = \sin\left(\tfrac{p}{2}\vartheta\right) \ , \tag{4.52}$$

as the $m(\vartheta)$ have maxima at ϑ^+ and minima at ϑ^-, satisfying $m(\vartheta^+) = -m(\vartheta^-)$.
The XY model's natural conjugated coordinate is the angle ϑ and therefore Equation 4.20 and

Equation 4.21 have to be adapted to rotary motion. The velocity is replaced by the angular velocity ω in this case.
Equation 4.49 yields the force

$$\begin{aligned}\frac{\partial V(\{\vartheta\})}{\partial \vartheta_{i,j}} = \quad & J_{\parallel} m\Big(\sin\left(\vartheta_{i,j} - \vartheta_{i+1,j}\right) + \sin\left(\vartheta_{i,j} - \vartheta_{i-1,j}\right) \Big) \\ & + J_{\perp} m\Big(\sin\left(\vartheta_{i,j} - \vartheta_{i,j+1}\right) + \sin\left(\vartheta_{i,j} - \vartheta_{i,j-1}\right) \Big) \\ & + hp \sin(p\vartheta_i) \ .\end{aligned} \tag{4.53}$$

Eventually, the Langevin equations become

$$\frac{\mathrm{d}}{\mathrm{d}t}\vartheta_{i,j}(t) = \omega_{i,j}(t) \ , \tag{4.54}$$

$$\frac{\mathrm{d}}{\mathrm{d}t}\omega_{i,j}(t) = -\frac{\eta}{I}\omega_{i,j}(t) - \frac{1}{I}\frac{\partial V(\{\vartheta\})}{\partial \vartheta_{i,j}} + \sqrt{\frac{2k_B T\eta}{I^2}}\Gamma(t) \ , \tag{4.55}$$

with the moment of inertia I replacing the mass m. The implementation of the integration of this coupled set of stochastic differential equations will be the subject of the next section.

5 Implementation and Results

To reduce finite size corrections it is beneficial to consider as large systems as possible. Combined with the critical slowing down described in Section 3.4 the problem at hand inherently generates an arbitrarily large computational cost. On top comes the stochastic nature of the system, requiring to run many simulations to extract ensemble averages, as well as the need to avoid discretization errors and ensure convergence when implying ?? by choosing a small dt. This makes an efficient and fast implementation a crucial part of our investigations.

5.1 GPU programming

Besides the difficulties just described, there is an advantage that can be made use of. The langevin equations for the different lattice sites may be coupled through the potential Equation 4.53, but the integration step for $t + dt$ only depends of the $\vartheta_{i,j}(t)$ of the previous step, meaning that the integrations can be performed simultaneously. This allows for heavy parallelization, making the problem predestined for a GPU implementation.

The main difference between a conventional single core implementation on a central processing unit (CPU) and one on a graphical processing unit (GPU) is the number of processing cores involved. While CPUs only have few (~ 10) powerful processing cores, GPUs are made up of more than $\sim 10^4$ cores. The CPU solves problems in a sequential matter, doing calculation after calculation making it suitable for usecases where the next step directly depends on the on before. In contrast, the GPU is able to perform many independent calculations real time simultaneously on its different cores. In situations where this is applicable, GPU implementations yield a significant speedup of up to a factor of 10^3. A concept of the different solution approaches is shown in Figure 5.1.

For performance reasons the implementation took place (?) in `C++` using `Thrust` [67] as high level interface for Nvidia's parallel computing platform `Cuda` [54]. The source code can be found at `https://github.com/andiw99/Master-Arbeit`. The architecture is inspired by Ahnert et al.'s work [2].

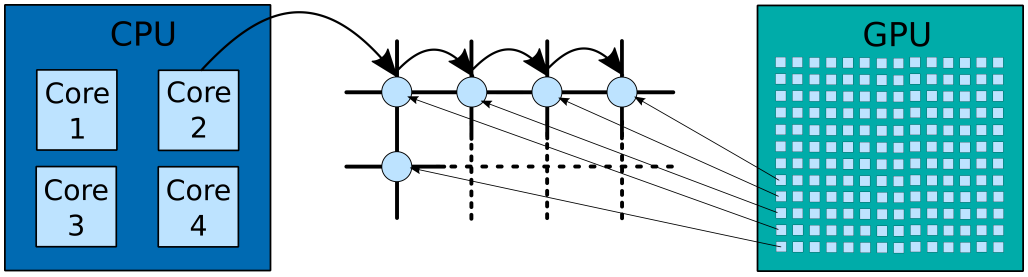

Figure 5.1: A CPU using single core processing would integrate the langevin equation for lattice site i and move on to site $i+1$. The use of multi core processing would allow the CPU to integrate 4 sites simultaneously. In contrast, using GPU programming enables to evaluate the langevin equation at about $10^4 - 10^5$ sites at the same time.

5.2 Benchmarks

Since an analytic solution of our model is intractable, proper benchmarks are vital to ensure the correctness of our simulation. Furthermore the stepsize used in ?? has to be analyzed to ensure convergence as well as a balance between the discretization error and efficiency.
The Benchmarks that were conducted are

- the statistics of independent harmonic oscillators with thermal coupling,
- the equilibrium distribution of particles in a cosine potential,
- the equilibrium distribution of a system composed of two particles in a cosine potential with cosine interaction

The equation that describes the time evolution of probability densities of brownian motion is the **Fokker-Planck equation**. When talking about the probability density $p(x, v, t)$ in terms of particle velocity v and position x it is often referred to as the **Klein-Kramers-** or **Smoluchowski** equation and written as

$$\frac{\partial}{\partial t}p(x,v,t) = \left(-\frac{\partial}{\partial x}v + \frac{\partial}{\partial v}\left(\eta v - \frac{1}{m}\frac{\partial}{\partial x}V(x)\right) + \frac{\eta k_B T}{m}\frac{\partial}{\partial v^2}\right)p(x,v,t)\ . \tag{5.1}$$

The Fokker-Planck equation and the langevin equations (Equation 4.20 and Equation 4.21) are virtually identical and can be converted into each other. Ensemble averages over paths of langevin equations result in the probability distribution satisfying Equation 5.1. The steady state distribution of the Fokker-Planck equation is the canonical distribution

$$p(x,v) \propto e^{\beta\left(\frac{1}{2}mv^2 + V(x)\right)}, \tag{5.2}$$

allowing for an easy way to verify long term behavior.

5.2.1 Thermal harmonic oscillators

For a quadratic potential

$$V(x) = \tfrac{1}{2}\omega^2 x^2, \tag{5.3}$$

the Fokker-Planck equation is analytically solvable [63]. This makes it ideal to confirm correct dynamics of the simulation. The analytic solution for the second moment of $x(t)$ reads

$$\left\langle x^2 \right\rangle (t) = \frac{\eta k_B T}{m(\lambda_+ - \lambda_-)^2} \left[\frac{\lambda_+ + \lambda_-}{\lambda_+ \lambda_-} + \frac{4}{\lambda_+ + \lambda_-} \left(e^{-(\lambda_+ + \lambda_-)t} - 1 \right) - \frac{1}{\lambda_+} e^{-2\lambda_+ t} - \frac{1}{\lambda_-} e^{-2\lambda_- t} \right], \tag{5.4}$$

with

$$\lambda_\pm = \frac{1}{2} \left(\eta \pm \sqrt{\eta^2 - 4\omega^2} \right) \tag{5.5}$$

In Figure 5.2 we compare $\langle x^2 \rangle (t)$ calculated from $\approx$ 65000 path, simulated by either the Euler-Maruyama- or the BBK method, with the theoretical result. The BBK algorithm with $dt = 0.05$ and the Euler-Maruyama method with $dt = 0.001$ yield similar small deviations from the theoretical curve, suggesting that the BBK method can be used up to much larger stepsizes. Besides, the validity of both methods for thermal harmonic oscillators is given for both methods for small enough stepsizes.

5.2.2 Particles in a cosine potential

Another valuable Benchmark is the edge case of weakly interacting particles with $J = 0$. We will confirm that probability distribution calculated from ??? particle paths will approach the theoretical equilibrium distribution given by inserting Equation 4.49 for $J_\delta = 0$ into Equation 5.2.

In Figure 5.3 we show the calculated integrated probability density $p(x) = \int p(x, v) dv$ is plotted. The BBK method shows virtually no discretization errors up to a stepsize of $dt = 0.05$. For the Euler-Maruyama method large discretization errors show up for stepsizes one magnitude smaller.

Again, for sufficiently small stepsizes the long term behavior of our simulation is verified.

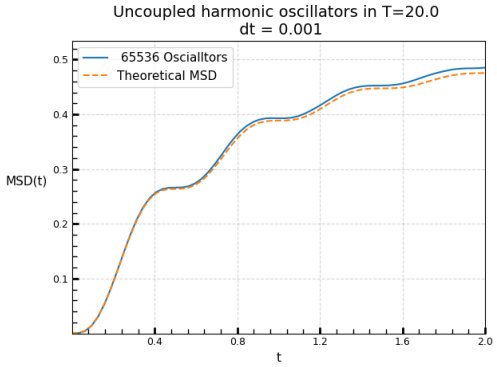

(a) The Euler-Maruyama method with a stepsize of $dt = 0.001$ results in small but noticeable deviations.

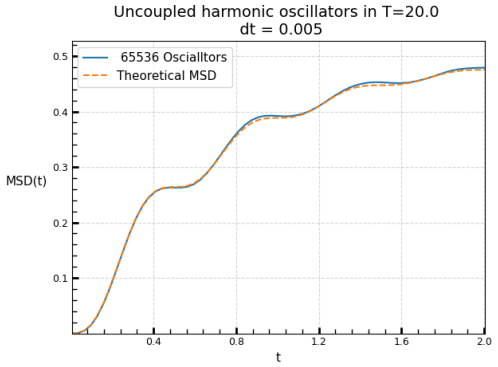

(b) The BBK method with a stepsize of $dt = 0.005$ reproduces the theoretical curve very well.

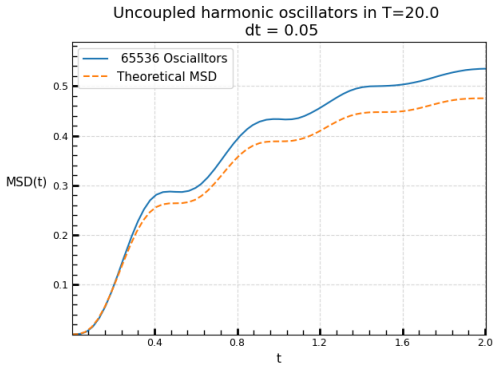

(c) The Euler-Maruyama method with a stepsize of $dt = 0.05$ results in large deviations.

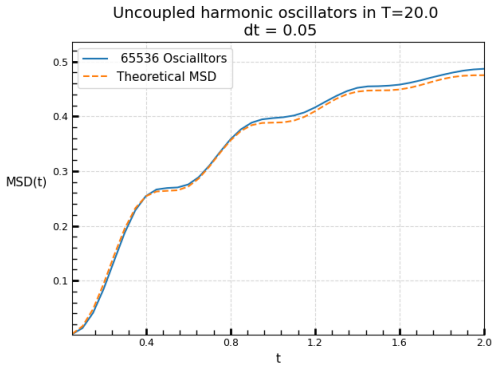

(d) The BBK method with a stepsize of $dt = 0.05$ results in small but noticeable deviations.

Figure 5.2: The calculated $\langle x^2 \rangle (t)$ of thermal harmonic oscillators are compared for the Euler-Maruyama- and the BBK method with different stepsizes

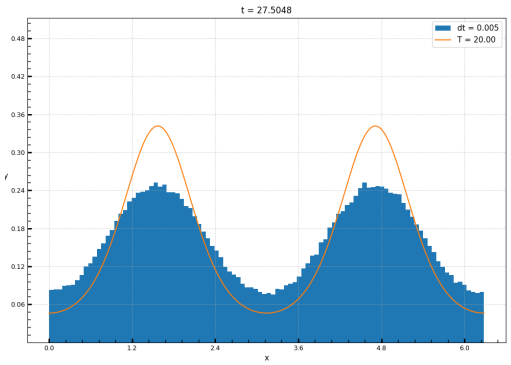

(a) The Euler-Maruyama method shows significant discretization errors regarding $p(x)$ even for a comparatively small stepsize of $dt = 0.005$.

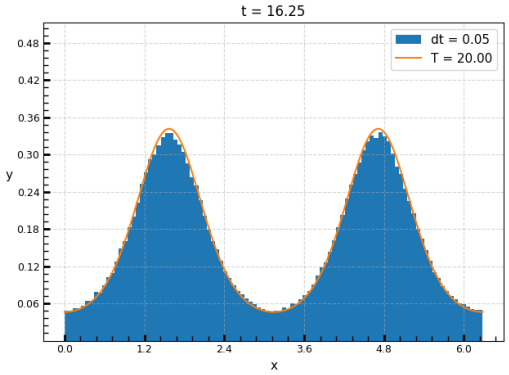

(b) The BBK method shows almost no deviation from the theoretical $p(x)$ even for a stepsize of $dt = 0.05$.

Figure 5.3: The integrated probability distributions $p(x)$ calculated from ??? particle paths are compared to the theoretical equilibrium distribution for the Euler-Maruyama method and the BBK Algorithm. It was made sure that the systems were completely relaxed, meaning that the effects of the starting position vanished and the shape of the probability distribution did not change anymore.

5.2.3 Two interacting particles in a cosine potential

The third benchmark has the purpose of verifying the correct behavior of the interaction. Since the equilibrium distribution becomes a high dimensional function $p(\{x_i\}, \{v_i\})$, a suitable representation is possible in the case of system consisting of two particles. The object of examination is again the equilibrium probability distribution of the Fokker-Planck equation.

In Figure 5.4 we now show cuts of the integrated probability density $p(x_1, x_2) = \int p(x_1, x_2, v_1, v_2) dv_2 dv_1$ with a constant x_2. It is verified that simple interacting systems are driven to their equilibrium by the method of langevin integrations. The statistical- and discretization errors vanish for many samples and small stepsizes.

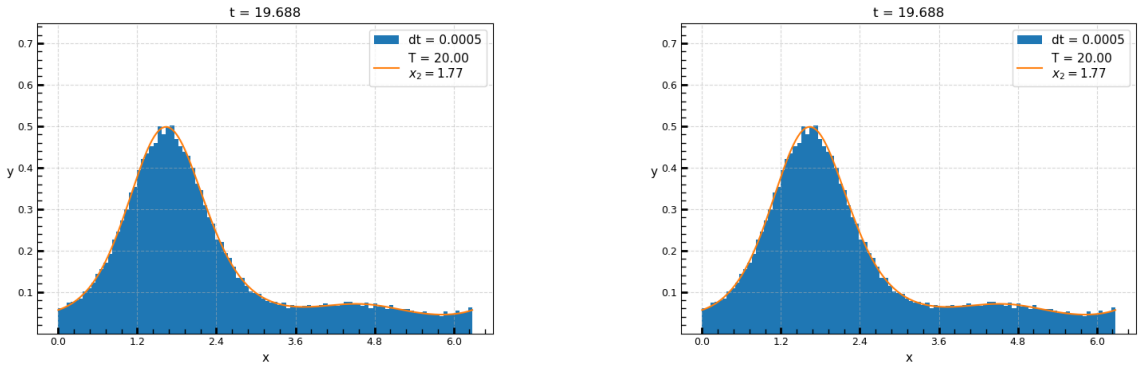

(a) Different x2s? **(b)** Different Temperatures?

Figure 5.4: Cuts of the integrated probability distributions $p(x_1, x_2)$ with a constant x_2 calculated from ??? particle paths are compared to the theoretical equilibrium distribution. It was made sure that the systems were completely relaxed, meaning that the effects of the starting position vanished and the shape of the probability distribution did not change anymore.

5.3 Results

In the following the results of the explained simulation will be presented. We will start with the examination of the critical exponents of our model.

The parameters will be measured in units of $J_\perp = 1$ and the initially used ratio $J_\parallel/J_\perp = 31.1$ is the one from Brand et. al [10]. The external field $h = 5$ is chosen small compared to $J_\parallel$ to ensure approximate validity of Equation 4.48. The strength of h should not influence the kind of phase transition we observe as long as it is finite, but may influence T_c. Both coupling strengths are negative to reproduce the c(4x2) symmetry. To conclude, as long as not otherwise stated, the in the following used model parameters of Equation 4.49 are

$$J_\perp = -1\ , \qquad J_\parallel = -31.1 \qquad \text{and} \qquad h = 5. \tag{5.6}$$

The dampening is set to $\eta = 1.5$. Our method of correlation length extraction Section A.2 works best if $\xi_\delta \ll L_\delta$. Since the Si(001) surface exhibits a large correlation length anisotropy $\frac{(\xi_\parallel/a_\parallel)}{(\xi_\delta/a_\delta)} \approx 10$, it is useful to ensure that the system sizes share a similar ratio. This way we can analyze larger correlation lengths without increasing the computational cost. The following systems have a ratio of $\frac{L_\parallel}{L_\perp} = 8$ if not stated otherwise. The used stepsize is $dt = 0.01$

5.3.1 static scaling

Since the phase transition of the Si(001) surface seems to belong to the Ising universality class [11], our simulation should reproduce this. The XY model with a p-fold symmetry breaking external field belongs to the Ising universality class for $p = 2$ [34], but the question remains if

this is still true for our adaptation (subsection 4.4.3) with a rational number $p \approx 2.57$.

Therefore, the finite size techniques and the Binder cumulant described in Section 3.3 and subsection 3.3.1 are employed to extract the critical exponent. The magnetization is calculated using Equation 4.52. We initialize totally ordered systems as suggested in [8], that is all dimers are alternatively buckled. We run multiple small independent systems simultaneously on a single GPU to achieve optimal parallelization. We run long simulations to ensure the thermalization of the systems. During the run, we document the Binder cumulant $U_L(t)$ to be able to afterwards determine a timepoint t_{equil} after which we judge the cumulant to be equilibrated. The cumulant is subject to statistical fluctuations, so to obtain useful averages it can be made use of the ergodic hypotheses. Instead of running many simulations and averaging the latest value of U_L, we simulate systems for long times t_{long} and calculate the ensemble average as the time average

$$\overline{U}_L = \frac{1}{(t_{long} - t_{equil})} \int_{t_{equil}}^{t_{long}} U_L(t) dt \ . \tag{5.7}$$

In Figure 5.5 the results for ??? systems simulated until t_{long} =??? are shown for temperatures very close to T_c. The critical point was approached by estimating the critical temperature with Equation 4.48 yielding $T_c^{est} \approx 0.618$, examining the general area for the phase transition and then iteratively closing in. The more precise T_c shall be determined, the closer the temperatures have to lie at T_c. The closer two temperatures lie, the easier it is for statistical fluctuations to smear their relative position and therefore the more averages you need. The same is true for the calculation of the critical exponent ν. The derivative $\frac{\partial U_L}{\partial \varepsilon}$ is calculated through a simple central difference. Afterwards the function Equation 3.42 is fitted to $\frac{\partial U_L}{\partial \varepsilon}(L)$. The result $\nu = 1.04$ is in good agreement with the theoretical critical exponent of the Ising model $\nu = 1$. The matching of the static critical exponent verifies our numerics as well as the assumption that our modification of the XY model still belongs to its expected universality class.

In Figure 5.6 the relation of the binder cumulant intersection aka our estimate for T_c is shown in dependence of the system size. The datapoints show the intersection of two curves $U_{L_1}(T)$ and $U_{L_2}(T)$ with $L_2 = 2L_1$. The errorbars are assumed to be $\Delta T_c = \frac{1}{2} dT$ with dT being the stepsize between the recorded temperatures. This error is probably an overestimation. The difference in $T_c(L_1, L_2)$ is negligable between $T_c(48, 96)$ and $T_c(64, 128)$ so we conclude that finite size effects on the critical temperature determination vanish on these length scales. For $L_1 = 64$ the measurement was continued to minimize the stepsize to $dT/2$. A smaller dT leads to a systematically slightly larger T_c as the intersection is usually located at the convex part of $U_L(T)$.

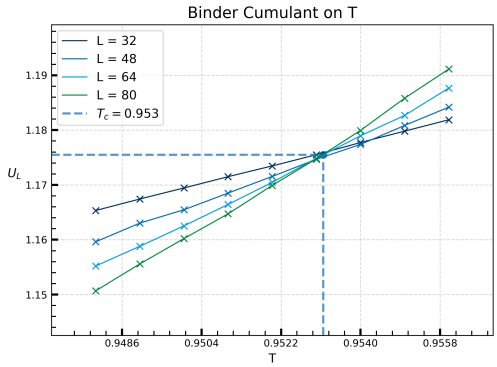

(a) The Binder cumulants intersect at $T_c = 0.953$. The intersection is determined by the minimum squared error between the cumulants.

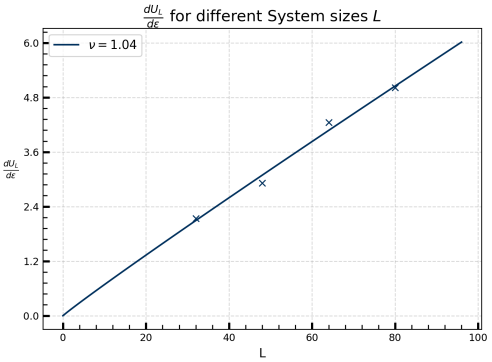

(b) The derivatives $\frac{\partial U_L}{\partial \varepsilon}$ scale like $\propto L^{\nu}$. The fitting results in $\nu = 1.04$ which is in good accordance with the Ising model.

Figure 5.5: The results for $\overline{U}_L$ of ??? averaged systems of different sizes simulated for a time of t_{long} =??? are shown. The estimated equilibration time is t_{equil} =???.

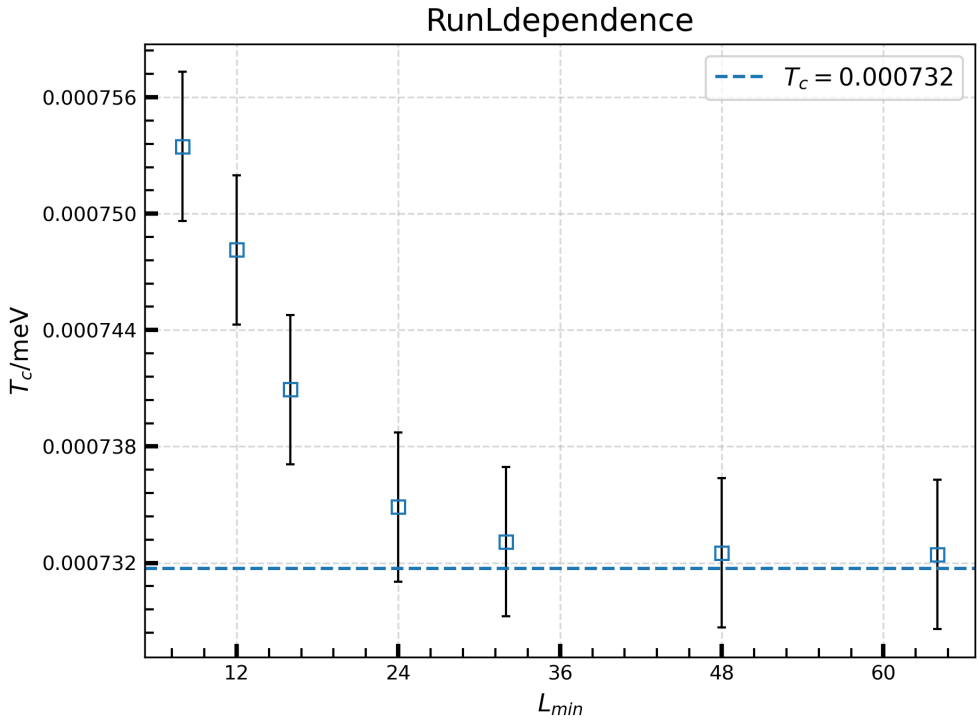

Figure 5.6: The dependence of the critical temperature T_c is calculated in dependence of the system size L. The x-axis shows the smaller system size L_{min}. The binder cumulant intersection is always calculated with twice the small system size $L_{max} = 2L_{min}$.

5.3.2 dynamic scaling

The dynamic universality classes are subgroups of the static universality classes and our model could very well be in a different dynamic universality class than the 2D Ising model. In the following multiple methods will be employed to extract the dynamic critical exponent z.

The Kibble-Zurek mechanism

The first method will be the extraction through Equation 3.51 and the Kibble-Zurek mechanism. Since we already gained knowledge of ν we can fit the exponent $\nu/(1+\nu z)$ to quenched correlation lengths deduce z.

The used quench protocol, i.e the manner in which the system is cooled down, will be a simple isotropic, linear quench like Equation 3.46. The starting temperature $\varepsilon(t_{start})$ is chosen to be sufficiently far away to observe adiabatic system evolution before crossing the freezeout point $\varepsilon(t_{start}) < \varepsilon(\hat{t})$. The end temperature $\varepsilon(t_{end})$ is chosen in symmetric distance from the transition point $|\varepsilon(t_{start})| = |\varepsilon(t_{end})|$.

In Figure 5.7 the results for the quench of our system are shown. A fit of the frozen correlation lengths $\hat{\xi}$ to Equation 3.51 is performed in **??** and **??**. Only the datapoints in the phase space where the Kibble-Zurek mechanism should be valid are used. It was made sure that $\hat{\xi}_\delta \ll L_\delta$ so that Section A.2 is still applicable. The extracted KZM exponent of $\nu/(1+\nu z)$ is unusually large and suggests that $z < 2$.

A KZM independent z extraction method is needed to verify the correct critical exponent.

Relaxation of the Binder cumulant

A simple way to examine the dynamic critical exponent is to consider the relaxation of the Binder cumulant including finite size scaling. This method was introduced by Li et. al [46] and will be used in the following to extract the dynamic critical exponent.

The basis is the time-resolved finite size scaling of the $(n)-$th moment of the magnetization

$$M^{(n)}(t,\varepsilon,L) = b^{-n\beta/\nu} M^{(n)}(b^{-z}t, b^{1/\nu}\tau, b^{-1}L) \ , \tag{5.8}$$

with $b = \frac{L}{L'}$ being the spatial rescaling factor. Janssen et. al [33] determined that the initial correlation length must be very short for Equation 5.8 to be valid. Therefore the investigated systems will be prepared in a high temperature, low order state. Following the definition of the Binder cumulant Equation 3.40, one can relate the Binder cumulant of systems of different

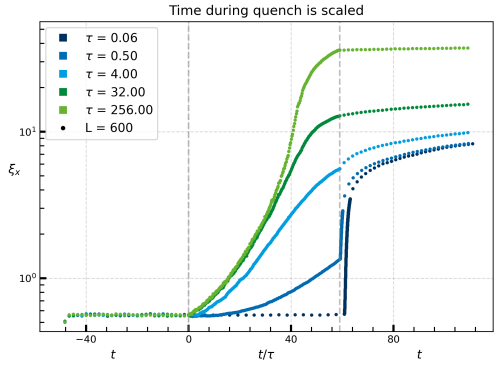

(a) The time-resolved quench-process $\xi_x(t)$ for different quench timescales is shown for the system sizes $L_x = 600, 1200$.

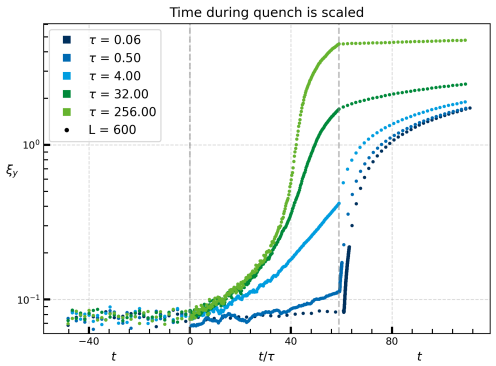

(b) The time-resolved quench-process $\xi_x(t)$ for different quench timescales is shown for the system sizes $L_y = 75, 150$.

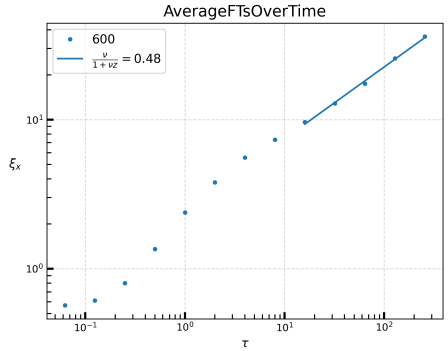

(c) The frozen correlation length $\hat{\xi}_x(\tau)$ depending on the quench timescale is investigated. A fit of the data to Equation 3.51 is calculated and drawn in the appropriate area.

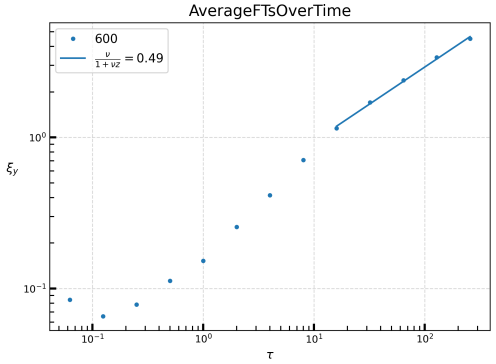

(d) The frozen correlation length $\hat{\xi}_y(\tau)$ depending on the quench timescale is investigated. A fit of the data to Equation 3.51 is calculated and drawn in the appropriate area.

Figure 5.7: The results of the quenches are investigated using the Kibble Zurek mechanism. The Kibble-Zurek mechanism is valid where the system is at the start of the quench able to adiabatically follow the process. When the quench is so fast that the system cannot follow the quench even at the start, the frozen correlation length is the equilibrium correlation length of the starting temperature and no scaling is observed.

sizes at the critical point $\varepsilon = 0$ by

$$U(t, 0, L_1) = U(b^{-z}t, 0, L_2) \ , \qquad \text{with} \qquad b = \frac{L_1}{L_2} \tag{5.9}$$

The exponent z is easily obtained by searching a time rescaling factor b^{-z} such that the recorded curves for U_{L_1} and U_{L_2} collapse. Since the sample systems are prepared in a high temperature state where $U_L = 3$, we expect a relaxation from this value to the equilibrium U_L^* which is, at $\varepsilon = 0$, the same for every system size. The results for the rescalings $32 \to 64$ and

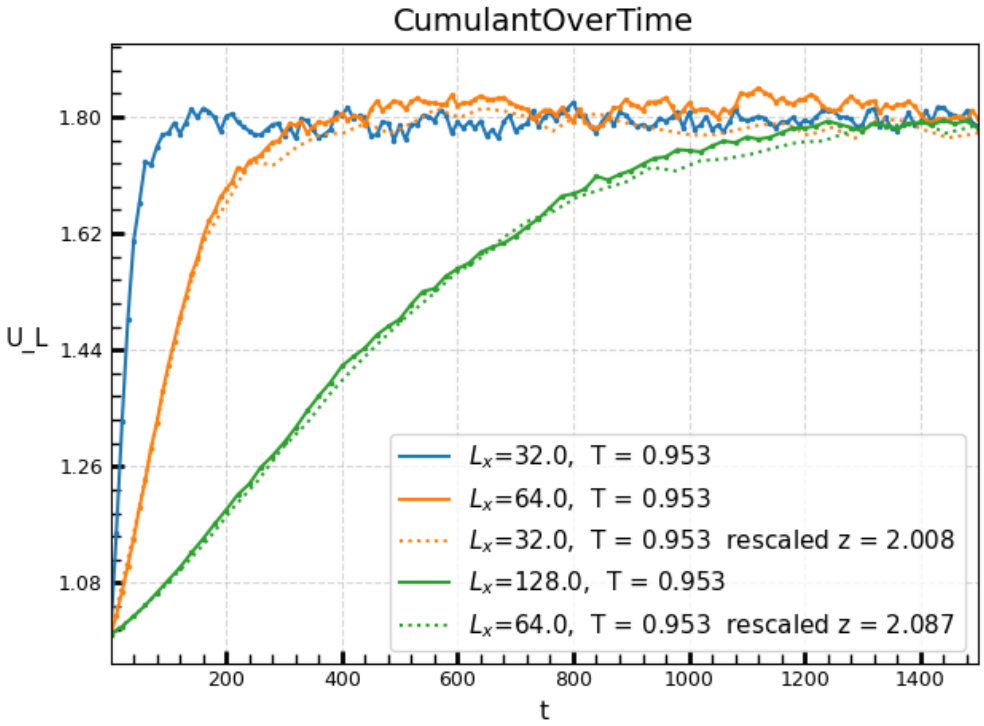

Figure 5.8: The best rescaling of $U_{L_1} \to U_{L_2}$ is selected by minimizing the squared error between the interpolated curves. The result of the rescaling from $64 \to 128$ yields a dynamic critical exponent of $z = 2.08$, close to the best known value for the Ising universality class (see **??**).

$64 \to 128$ calculated from ??? sample paths are shown in Figure 5.8. The rescaling $64 \to 128$ is to be trusted more than the $32 \to 64$ since it minimizes the finite size corrections to the scaling law Equation 5.8. Its result $z = 2.08$ is very close to the best available dynamical critical exponent of the Ising model $z_{Ising} = 2.14$.With this the calculated KZM exponent of $\nu/(1 + z\nu) = 0.33$ stands in harsh contradiction to the exponent obtained directly from the quench $\nu/(1 + z\nu) = 0.45$. Since it is from symmetry considerations very plausible that our model for silicon would show the Ising dynamical exponent, we would expect that the deviation stems from the Kibble-Zurek scaling. Since the system sizes used in the quenches is already very large, strong finite size corrections to the Kibble-Zurek scaling can be ruled out as cause of the deviation. The same is true for the discretization error of our stepsize since the same

quenches have been recalculated with a smaller stepsize. Since the correctness of our simulation has otherwise been verified, the most sensible explanation for the large Kibble-Zurek scaling exponent is that the cause has to be a systematic difference in the expected Kibble-Zurek mechanics (???). An idea could be the existence of subleading scalings like reported in [41] caused by other scaling fields than the temperature. In our case such a scaling field could be the strength of the external potential h.

In the following we will investigate the effect of the strength of h on the dynamical critical exponent as well as the Kibble-Zurek exponent.

5.3.3 The correlation length amplitudes ξ_δ^+

The static scaling law of the correlation length ξ_δ above the critical temperature ($\varepsilon > 0$) given by Equation 3.27 can be rewritten as

$$\xi_\delta(\varepsilon) = \xi_\delta^+ \varepsilon^{-\nu} \ , \tag{5.10}$$

with the so called correlation length amplitude ξ_δ^+. The + sign denotes the amplitude above the critical temperature. The correlation lengths in the Ising model are directly related to the temperature and the coupling constants J_δ. Their relation above the critical temperature is given by Equation 4.44. An expansion of Equation 4.44 around the critical temperature T_c leads to a simple relation between the coupling constants and the correlation length amplitudes,

$$\sinh\left(\frac{2|J_\delta|}{k_B T_c}\right) = \frac{\xi_\delta^+/a_\delta}{\xi_{\bar{\delta}}^+/a_{\bar{\delta}}} \ . \tag{5.11}$$

This relation is exceptionally useful, as it can be used to determine the coupling energies J_δ from the measured correlation lengths and critical temperatures as is done in [10], [11]. The value that is obtained here for the amplitude ratio in units of the lattice constants is $(\xi_\parallel^+/a_\parallel)/(\xi_\perp^+/a_\perp) = 10.3$.

A relation like Equation 5.11 for the XY model with a symmetry breaking field is not known at the moment and efforts to derive one were unsuccessful. So a direct relation of the correlation length ratio to the model couplings J_δ, h and even p is not possible. But since the symmetry broken XY model and the Ising model have shown to behave quite similar in the previous investigations, it is reasonable to examine the correlation length amplitude ratio for the Ising coupling constant ratio $J_\parallel/J_\perp = 31.1$.

The amplitude ratio is investigated by preparing the system in a random state and letting

it relax at a fixed temperature $T \gtrsim T_c$. To judge whether the system is relaxed and at the same time obtain a precise value for the equilibrium correlation length, ξ is monitored on the run in the spirit of Equation 5.7. Every $n_s = 100$ steps, ξ_δ is calculated and saved. After reaching a minimum step threshold, every $n_\sigma = 5n_s$ steps also the mean $\overline{\xi}_\delta$ as well as its error $\sigma_{\overline{\xi}_\delta}$ is calculated. The correlation of $\xi(t)$ and $\xi(t + n_s dt)$ has to be taken into consideration if $n_s dt < \tau$ (see Section A.3). When calculating mean and error, a fraction $p_\tau = 1/2$ of correlation lengths is ignored in order to account for the equilibration of the system. After falling below a maximum relative error of $\sigma_{max}/\overline{\xi}_\delta = 0.01$ for both directions, the run is terminated. The used system size is chosen as large as numerically feasible to minimize finite size effects around the critical temperature T_c.

The results for the equilibrium ξ_δ for a system of size L_x =?are shown in Figure 5.9. To

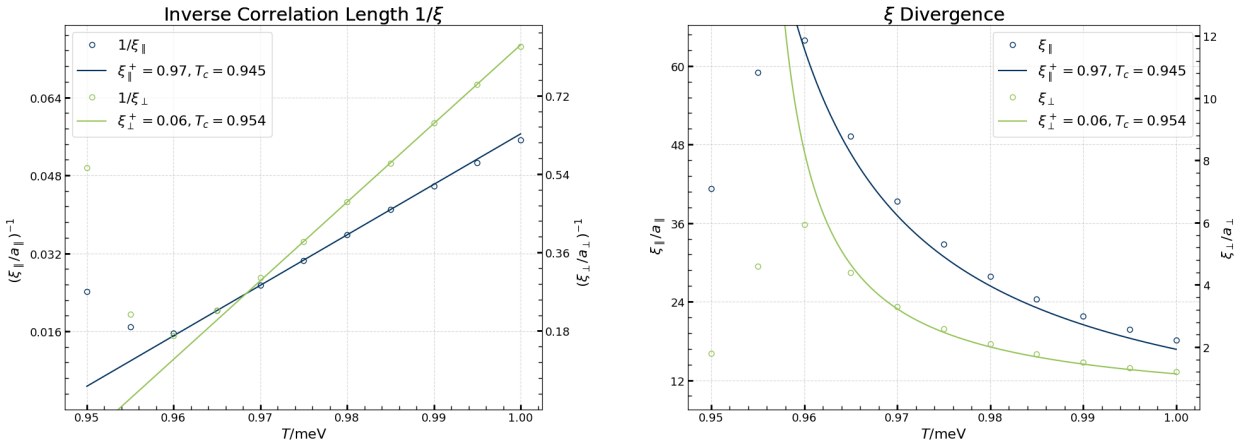

Figure 5.9: (a) The inverse correlation length ξ^{-1} of a system of size L_x =? equilibrium is measured and shown for temperatures $T \gtrsim T_c$. The line is a linear fit with the parameters ξ_δ^+ and T_c. **(b)** The divergence of ξ is measured around $T \gtrsim T_c$. The line is calculated by Equation 5.10, using the parameters obtained by the fit of (a).

extract the correlation length amplitude ξ_δ^+, the scaling of ξ_δ^{-1} was considered, which is given by

$$\xi_\delta^{-1}(T) = \frac{1}{\xi_\delta^+}\left(\frac{T - T_c}{T_c}\right) = -\frac{1}{\xi_\delta^+} + (T_c\xi_\delta^+)^{-1}T \ , \tag{5.12}$$

if the result $\nu = 1$ is used. Therefore ξ behaves linearly in T around the critical point. Which datapoints shall be included is decided by selecting the best linear regression in the parameters of ξ_δ^+ and T_c of at least 4 consecutive datapoints that agree with the previously determined critical temperature $T_c^{U_L}$. The quality of the fit is determined by the r^2-value of the regression. A minimum r^2-value of $r^2_{min} = 0.98$ is required to accept a successful fit. (TODO) maybe just choose the regression that has a minimum r^2 value and is as close to Tc as possible?) Close to T_c finite size effects become visible. To illustrate this, ξ is recalculated at the questionable datapoints for a system of size $L'_x = 2L_x$. At this point I am not sure why the correlation

length becomes smaller already a temperatures slightly larger than T_c, the RG theory actually predicts that the maximum of ξ should be shifted to a lower temperature?. The correlation length ratio of $\xi_{\parallel}^{+}/\xi_{\perp}^{-} =?$ is smaller than expected for the Ising model. Reasons for this could be influences of the symmetry breaking field and structural difference in the relationship of the coupling constants and the correlation lengths. The influence of the symmetry breaking field on the amplitude ration will be investigated in the following.

5.3.4 quantitative

Since the dimer interaction is a kind of dipole interaction [57], our XY-model interaction might not reproduce quantitative results of the real system. In the following some quantitative considerations will be done anyway.

Since the numbers used in a simulation are all dimensionless, one has to think about what those numbers represent in physical quantities. Since the mass m, or for rotational motion equivalently the moment of inertia I, is not implemented into the simulation, it is easiest to measure all quantities in multiples of I. Natural units will be used in the following. The moment of inertia is approximated as two point masses $m_{Si} \approx 28u = 26$ GeV with a distance of $2r \approx 2$ Å ≈ 10 keV^{-1}, yielding

$$I \approx 2m_{Si}r^2 \approx 2\,(26\text{ GeV})\left(5\text{ keV}^{-1}\right)^2 = 1300\text{ meV}^{-1}\ . \tag{5.13}$$

The dimensionless angular velocity Ω in units of I is

$$\Omega(t) = I\omega(t)\ . \tag{5.14}$$

The dimensionless version of Equation 4.55 becomes

$$\begin{aligned}\Omega_{i,j}(t+dt) &= \Omega(t) - \eta\Omega_{i,j}(t)\frac{dt}{I} - I\frac{\partial V(\{\vartheta\})}{\partial\vartheta_{i,j}}\frac{dt}{I} + \sqrt{\frac{2T\eta}{I^2}}n(t)I\sqrt{dt} \\ &= \Omega(t) - \eta\Omega_{i,j}(t)d\sigma - \frac{\partial v(\{\vartheta\})}{\partial\vartheta_{i,j}}d\sigma + \sqrt{2\kappa\eta}n(t)\sqrt{d\sigma}\ ,\end{aligned} \tag{5.15}$$

with the dimensionless quantities

$$\sigma = t/I, \tag{5.16}$$

$$v(\vartheta) = IV(\vartheta), \qquad \text{and} \tag{5.17}$$

$$\kappa = IT. \tag{5.18}$$

The second line of Equation 5.15 is what is implemented in the simulation. To get the physical values, the equation has to be divided by the moment of inertia I. The position coordinate ϑ of

the dimer however does not have to be converted since the dimensionless form of Equation 4.54

$$\begin{aligned}\vartheta(t+dt) &= \vartheta(t) + \Omega(t)d\sigma = \vartheta(t) + I\omega(t)\frac{dt}{I} \\ &= \vartheta(t) + \omega(t)dt\end{aligned} \tag{5.19}$$

equals the dimensionful form.

The used dimensionless stepsize of $d\sigma = 0.01$ corresponds to a physical stepsize of

$$dt = Id\sigma = 1300 \text{ meV}^{-1} \cdot 0.01 \approx 0.01 \text{ ns} , \tag{5.20}$$

which is very reasonable since this stepsize is of the order of magnitude of the fast hight temperature flipping of the dimers (source? BrandCritical). The dimensionless critical temperature has a value of

$$\kappa_c = 1300 \text{ meV}^{-1} \cdot 16.43 \text{ meV} \approx 22100 , \tag{5.21}$$

using the experimental critical temperature $T_c = 16.43$ meV of Brand et. al [10]. Assuming a ratio of $J_\parallel/J_\perp = 31$, Equation 4.48 can be used to together with T_c to estimate the values of J_δ. We get

$$J_\perp = 2.66 \text{ meV} \qquad \text{and} \qquad J_\parallel = 82.46 \text{ meV} , \tag{5.22}$$

corresponding to the dimensionless values $j_\delta = IJ_\delta$ of

$$j_\perp = 3580 \qquad \text{and} \qquad j_\parallel = 110980 . \tag{5.23}$$

The question now is how to choose h in order not to change the phase transition again. Therefore a perturbation based version of Equation 4.48 including h would be very useful. And the dampening is also crucial to the timescales on which the system evolves. There is probably no way of estimating this? Or there might be one but that is surely not possible in 2 months...
For the addition of h: you know the form of the phase diagram of the XY model, and I think you even know the kind of function it describes. What you probably don't know are the prefactors, etc. You can fit them but they probably are dependent on J? It is not dependent on η at least.

The equilibrium position of the dimers is determined by the strength of repulsion $J_\parallel$ and $J_\perp$, the amplitude of the symmetry breaking field h and the position of its minima determined by

the parameter p. In the case of ferromagnetic interaction, the equilibrium position is solely determined by $p = \frac{18}{7}$ which yields the experimental equilibrium position of $\vartheta^* = \frac{7}{18}\pi = 70°$ (measuring from the z-Axis). We can also infer that $p > 2$ as $p = 2$ means that the equilibrium position of the symmetry breaking field is at $\vartheta = \pi/2$, corresponding to a horizontal dimer. Since we see from DFT calculations that even the buckling itself without any constraint on the configuration decreases the energy, this is not realistic. The two constrains conclude to $p \in [2, 2.57]$ Consider now a specific lattice site of a system in total equilibrium, meaning that the site's buckling angle is $\vartheta = \vartheta^*$ and the buckling angle of all its neighbors is $\vartheta_{NN} = -\vartheta^*$. The condition that $\left.\frac{\partial H(\vartheta)}{\partial \vartheta}\right|_{\vartheta=\vartheta^*} = 0$ gives

$$-4\sin(4\vartheta^*)\left(\frac{J_\parallel + J_\perp}{h}\right) = p\sin\left(\vartheta^* p\right) \ . \tag{5.24}$$

This is a transcendental That determines the parameter p in dependence of the coupling constants, h and the desired equilibrium position. For the experimental ϑ^*, $\sin(4\vartheta^*) \approx -1$, leading to the simpler form

$$4\frac{J_\parallel + J_\perp}{h} = p\sin(\tfrac{7\pi}{18}p) \ . \tag{5.25}$$

The right hand side of this equation is monotonically decreasing on the interval $[2, 2.57]$, so a solution is only possible if

$$\frac{J_\parallel + J_\perp}{h} \leq \frac{1}{4}\cdot 2 \cdot \sin(\frac{14}{18}\pi) \approx \frac{1}{3} \tag{5.26}$$

Fitting the model parameters to DFT calculations

Numerous investigations calculated configuration energies of the Si(001) [22, 61] surface by density functional theory (DFT) methods and fitted the Ising model parameters accordingly [57, 31, 30, 73]. We can trace their path and use their configuration energies to get a feeling of the dimension of our coupling parameters.

The model in use has 4 parameters that influence the configuration energy, being the interaction couplings $J_\parallel, J_\perp$, the strength h and the position, characterized by p, of the symmetry breaking field. Another unknown is the binding energy of the lowest configuration E_0, in our case being the absolute energy of the $c(4\times 2)$ configuration. Since p is inside a $cos(p\theta)$, the fitting of the model parameters will result in a 5-dimensional non linear system of equations, which could be a bit tedious to solve. An approximation that is probably still fairly accurate would be to determine p solely from the equilibration angle of the asymmetric $p(2\times 1)_a$ configuration. Since in this configuration all dimers have the same buckling angle by definition, the dimer interaction cannot influence the equilibrium angle, since there is i.e. no repulsion involved that

could shift the minimum of the symmetry breaking field. The caveat is that we have to assume that the surface configuration does not or only slightly change the strength and shape of the symmetry breaking field, which is in the real world system generated by the silicon bulk. If that's the case, the angle that is observed in the $p(2\times1)_a$ configuration directly determines p since

$$\cos\left(\vartheta_{p(2\times1)_a}p\right)\approx -1 \qquad \Rightarrow \qquad p=\pi/\vartheta_{p(2\times1)_a}\ . \tag{5.27}$$

Pillay et. al [57] found an buckling angle of $\approx 17.2°$ resulting in $\vartheta_{p(2\times1)_a}=72.8°$ and $p=2.473$. With this simplification we obtain a linear system of equations

$$c(4\times2): \quad \cos(4\vartheta^{(1)}) \quad J_\parallel+\cos(4\vartheta^{(1)}) \quad J_\perp+\cos\left(\vartheta^{(1)}p\right)h=E_0 \tag{5.28}$$
$$p(2\times2): \quad \cos(4\vartheta^{(2)}) \quad J_\parallel+ \quad J_\perp+\cos\left(\vartheta^{(2)}p\right)h=E_0+E_{p(2\times2)} \tag{5.29}$$
$$p(2\times1)_a: \quad J_\parallel+ \quad J_\perp+\cos\left(\vartheta^{(3)}p\right)h=E_0+E_{p(2\times1)} \tag{5.30}$$
$$p(4\times1): \quad J_\parallel+\cos\left(4\vartheta^{(4)}\right) \quad J_\perp+\cos\left(\vartheta^{(4)}p\right)h=E_0+E_{p(4\times1)} \tag{5.31}$$

I am not sure whether the NN interaction describes the (4×1) (or some other configurations) correctly. I think that $J_\perp$ is effectively antiferromagnetic is only valid in the c(4x2) configuration. I think the equations for $p(2\times1)_a$ and $p(4\times1)$ are just wrong and have to include diagonal interactions. This would add another parameter to my calculation and I would need another configuration energy. Including NNN interactions, so the diagonal interaction $J_\times$ we get for the system of equations from above: WAIT this is wrong right? The J_x should not have the cosine prefactor in the first line since the diagonal neighbors have the same buckling angle

$$\cos(4\vartheta^{(1)})J_\parallel+\cos(4\vartheta^{(1)}) \quad J_\perp- \quad 2\cos(4\vartheta^{(1)})J_\times+ \quad \cos\left(\vartheta^{(1)}p\right)h=E_0 \tag{5.32}$$
$$\cos(4\vartheta^{(2)})J_\parallel+ \quad J_\perp- \quad 2J_\times+ \quad \cos\left(\vartheta^{(2)}p\right)h=E_0+E^{(2)} \tag{5.33}$$
$$J_\parallel+ \quad J_\perp+ \quad 2J_\times+ \quad \cos\left(\vartheta^{(3)}p\right)h=E_0+E^{(3)} \tag{5.34}$$
$$J_\parallel+\cos\left(4\vartheta^{(4)}\right) \quad J_\perp+ \quad 2\cos(4\vartheta^{(4)})J_\times+ \quad \cos\left(\vartheta^{(4)}p\right)h=E_0+E^{(4)} \tag{5.35}$$
$$J_\parallel+ \quad J_\perp+ \quad 2J_\times+ \quad \cos\left(\frac{\pi}{2}p\right)h=E_0+E^{(5)} \tag{5.36}$$

$$\cos(4\vartheta^{(1)})J_\parallel+\cos(4\vartheta^{(1)}) \quad J_\perp+ \quad 2J_\times+ \quad \cos\left(\vartheta^{(1)}p\right)h=E_0 \tag{5.37}$$
$$\cos(4\vartheta^{(2)})J_\parallel+ \quad J_\perp+ \quad 2\cos(4\vartheta^{(2)})J_\times+ \quad \cos\left(\vartheta^{(2)}p\right)h=E_0+E^{(2)} \tag{5.38}$$
$$J_\parallel+ \quad J_\perp+ \quad 2J_\times+ \quad \cos\left(\vartheta^{(3)}p\right)h=E_0+E^{(3)} \tag{5.39}$$
$$J_\parallel+\cos\left(4\vartheta^{(4)}\right) \quad J_\perp+ \quad 2\cos(4\vartheta^{(4)})J_\times+ \quad \cos\left(\vartheta^{(4)}p\right)h=E_0+E^{(4)} \tag{5.40}$$
$$J_\parallel+ \quad J_\perp+ \quad 2J_\times+ \quad \cos\left(\frac{\pi}{2}p\right)h=E_0+E^{(5)} \tag{5.41}$$

where we added another equation for the $p(2\times1)_s$ configuration where the its angle is defined to be $\vartheta^{(5)} = \pi/2$. We need that one as we have to determine another coupling constant now. We could use the values from Inoue et al. as they have those 5 configurations that we want to use, but I am not sure whether those values are accurate and we don't really know the angles, we only know the Δz displacement but not the bond length. We can eliminate E_0 from the equations by subtracting the $c(4\times2)$ configuration energy to obtain:

$$\begin{aligned}
0 \quad & J_\parallel + \quad (1-\cos(4\vartheta))J_\perp \quad + 2\,(\cos(4\vartheta)-1) \quad J_\times + \quad 0h \quad = E_{p(2\times2)} & (5.42)\\
(1-\cos(4\vartheta)) \quad & J_\parallel + \quad 0J_\perp \quad + 2\,(\cos(4\vartheta)-1) \quad J_\times + \quad 0h \quad = E_{p(4\times1)} & (5.43)\\
(1-\cos(4\vartheta)) \quad & J_\parallel + \quad (1-\cos(4\vartheta))J_\perp \quad + \quad 0 \quad J_\times + \quad 0h \quad = E_{p(2\times1)} & (5.44)
\end{aligned}$$

Fitting yields

$$\begin{aligned}
J_\parallel &= 115.6 \text{ meV} \Rightarrow \qquad j_\parallel = 150000 & (5.45)\\
J_\perp &= -17.3 \text{ meV} & (5.46)\\
J_\times &= -9.5 \text{ meV} & (5.47)\\
J_\perp^{eff} &= J_\perp - 2J_\times = 1.8 \text{ meV} \Rightarrow j_\perp = 2340 & (5.48)
\end{aligned}$$

Dabrowski and Scheffler [16] describe the movement of the dimer to be in a double well potential with a barrier height of $E_B = 100$ meV. The same argumentation can be applied to [31] leading to $E_B = 170$ meV. In our model the potential barrier can be specified as

$$h\,(1+\cos\left(p\frac{\pi}{2}\right)) = E_B\ . \tag{5.49}$$

Together with Equation 5.24 we have two more equations at hand to determine the location of the minimum p and strength h of the symmetry breaking field. Fitting with the E_B value of Inoue et. al yields

$$\begin{aligned}
h &= 1324 \text{ meV} \Rightarrow h_{num} = 1722500 & (5.50)\\
p &= 2.33 & (5.51)
\end{aligned}$$

New P. Kratzer Mail hat Dimer row consisting of 5 dimers and a domain boundary which they then advanced. The advance takes place by flipping the dimer at the domain boundary, in which the dimer takes on a horizontal position. The energy difference between the domain

boundary state and the horizontal state is

$$\begin{aligned} E_H - E_{DB} &= 74 \text{ meV} \\ &= h\left(\cos(\pi/2p) - \cos(\vartheta p)\right) \\ &\quad + J_{\parallel}\left(2\cos(2(\vartheta - \pi/2)) - 1 - \cos(4\vartheta)\right) \\ &\quad + 2J_{\times}\left(\cos(\pi + 2\vartheta) - 1 - \cos(4\vartheta)\right) \end{aligned} \tag{5.52}$$

Fitting with values from P. Kratzer yields

$$h = 893 \text{ meV} \Rightarrow h_{num} = ... \tag{5.53}$$

$$p = 2.21 \tag{5.54}$$

The numerical values are very large, this would mean that we would have to decrease the stepsize to ensure numerical stability, but then the quenches and stuff would take a really short time in real time? Is this a problem? The equilibration and stuff should not take longer right because everything should be scale invariant. If we calculate the critical temperature that the bare XY model would have with the current values we would get

$$\kappa_c = 24620 \qquad \Rightarrow \qquad T_c = 18.94 \text{ meV} \tag{5.55}$$

5.3.5 other

5.4 Discussion

6 Summary and Lookout

6.1 Summary

6.2 Lookout

A Appendix

A.1 Caldeira-Legget calculation

Starting point for this calculation is Equation 4.32. Consider the trace in the second term in Equation 4.32:

$$\mathrm{tr}_B\left\{\left[\hat{H}_I,\left[\hat{\boldsymbol{H}}_I(-\tau),\hat{\rho}_S(t)\otimes\overline{\rho}_B\right]\right]\right\}=\mathrm{tr}_B\left\{\left[\hat{x}\otimes\hat{B},\left[\hat{\boldsymbol{x}}(-\tau)\otimes\hat{\boldsymbol{B}}(-\tau),\hat{\rho}_S(t)\otimes\overline{\rho}_B\right]\right]\right\}\ . \tag{A.1}$$

Multiplying out the commutator yields

$$\begin{aligned}(\text{A.1})\ =\mathrm{tr}_B\Big\{&+\hat{x}\hat{\boldsymbol{x}}(-\tau)\hat{\rho}_S(t)\otimes\hat{B}\hat{\boldsymbol{B}}(-\tau)\overline{\rho}_B-\hat{x}\hat{\rho}_S(t)\hat{\boldsymbol{x}}(-\tau)\otimes\hat{B}\ \overline{\rho}_B\hat{\boldsymbol{B}}(-\tau)\\&-\hat{\boldsymbol{x}}(-\tau)\hat{\rho}_S(t)\hat{x}\otimes\hat{\boldsymbol{B}}(-\tau)\overline{\rho}_B\hat{B}+\hat{\rho}_S(t)\hat{x}\hat{\boldsymbol{x}}(-\tau)\otimes\overline{\rho}_B\hat{\boldsymbol{B}}(-\tau)\hat{B}\Big\}\ .\end{aligned} \tag{A.2}$$

The factors belonging to the Hilbert space of the system can be pulled out of the trace. Additionally we use the cyclic property of the trace as well as the expectation value representation $\left\langle\hat{A}\right\rangle=\mathrm{tr}\left(\hat{A}\rho\right)$ to obtain

$$\begin{aligned}(\text{A.2})=\ &\left(\hat{x}\hat{\boldsymbol{x}}(-\tau)\hat{\rho}_S(t)-\hat{\boldsymbol{x}}(-\tau)\hat{\rho}_S(t)\hat{x}\right)\left\langle\hat{B}\hat{\boldsymbol{B}}(-\tau)\right\rangle\\&+\left(\hat{\rho}_S(t)\hat{\boldsymbol{x}}(-\tau)\hat{x}-\hat{x}\hat{\rho}_S(t)\hat{\boldsymbol{x}}(-\tau)\right)\left\langle\hat{\boldsymbol{B}}(-\tau)\hat{B}\right\rangle\ .\end{aligned} \tag{A.3}$$

We can rewrite $\langle\hat{B}\hat{\boldsymbol{B}}(-\tau)\rangle=\frac{1}{2}\langle[\hat{B},\hat{\boldsymbol{B}}(-\tau)]+\{\hat{B},\hat{\boldsymbol{B}}(-\tau)\}\rangle$ and likewise $\langle\hat{\boldsymbol{B}}(-\tau)\hat{B}\rangle$ which yields

$$\begin{aligned}(\text{A.3})=&\frac{1}{2}\left\langle\left[\hat{B},\hat{\boldsymbol{B}}(-\tau)\right]\right\rangle\Big(+\hat{x}\hat{\boldsymbol{x}}(-\tau)\hat{\rho}_S(t)+\hat{x}\hat{\rho}_S(t)\hat{\boldsymbol{x}}(-\tau)-\hat{\boldsymbol{x}}(-\tau)\hat{\rho}_S(t)\hat{x}\\&\qquad-\hat{\rho}_S(t)\hat{\boldsymbol{x}}(-\tau)\hat{x}\Big)\\&\frac{1}{2}\left\langle\left\{\hat{B},\hat{\boldsymbol{B}}(-\tau)\right\}\right\rangle\Big(\hat{x}\hat{\boldsymbol{x}}(-\tau)\hat{\rho}_S(t)-\hat{x}\hat{\rho}_S(t)\hat{\boldsymbol{x}}(-\tau)-\hat{\boldsymbol{x}}(-\tau)\hat{\rho}_S(t)\hat{x}\\&\qquad+\hat{\rho}_S(t)\hat{\boldsymbol{x}}(-\tau)\hat{x}\Big)\ .\end{aligned} \tag{A.4}$$

The position operator terms can be combined to

$$[\hat{x}, \{\hat{\boldsymbol{x}}(-\tau), \hat{\rho}_S(t)\}] = \hat{x}\hat{\boldsymbol{x}}(-\tau)\hat{\rho}_S(t) + \hat{x}\hat{\rho}_S(t)\hat{\boldsymbol{x}}(-\tau) - \hat{\boldsymbol{x}}(-\tau)\hat{\rho}_S(t)\hat{x} - \hat{\rho}_S(t)\hat{\boldsymbol{x}}(-\tau)\hat{x} \quad \text{(A.5)}$$

$$[\hat{x}, [\hat{\boldsymbol{x}}(-\tau), \hat{\rho}_S(t)]] = \hat{x}\hat{\boldsymbol{x}}(-\tau)\hat{\rho}_S(t) - \hat{x}\hat{\rho}_S(t)\hat{\boldsymbol{x}}(-\tau) - \hat{\boldsymbol{x}}(-\tau)\hat{\rho}_S(t)\hat{x} + \hat{\rho}_S(t)\hat{\boldsymbol{x}}(-\tau)\hat{x} \ . \quad \text{(A.6)}$$

Plugging Equation A.5 into Equation A.4 yields for the trace of Equation A.2:

$$\begin{aligned} \mathrm{tr}_B \left\{ \left[\hat{H}_I, \left[\hat{\boldsymbol{H}}_I(-\tau), \hat{\rho}_S(t) \otimes \overline{\rho}_B\right]\right]\right\} = \frac{1}{2}\left\langle \left[\hat{B}, \hat{\boldsymbol{B}}(-\tau)\right]\right\rangle [\hat{x}, \{\hat{\boldsymbol{x}}(-\tau), \hat{\rho}_S(t)\}] \\ \frac{1}{2}\left\langle \left\{\hat{B}, \hat{\boldsymbol{B}}(-\tau)\right\}\right\rangle [\hat{x}, [\hat{\boldsymbol{x}}(-\tau), \hat{\rho}_S(t)]] \end{aligned} \quad \text{(A.7)}$$

We will now try to find expressions for $\langle[\hat{B}, \hat{\boldsymbol{B}}(-\tau)]\rangle$ and $\langle\{\hat{B}, \hat{\boldsymbol{B}}(-\tau)\}\rangle$. The interaction picture operator $\hat{\boldsymbol{B}}(-\tau)$ can be calculated by it's definition

$$\begin{aligned} \hat{\boldsymbol{B}}(-\tau) = e^{i\hat{H}_B(-\tau)}\hat{B}e^{-i\hat{H}_B(-\tau)} &= e^{i\hat{H}_B(-\tau)} \sum_n \kappa_n \sqrt{\frac{\hbar}{2m_n\omega_n}} \left(\hat{b}_n + \hat{b}_n^\dagger\right) e^{-i\hat{H}_B(-\tau)} \\ &= \sum_n \kappa_n \sqrt{\frac{\hbar}{2m_n\omega_n}} \left(\hat{\boldsymbol{b}}_n(-\tau) + \hat{\boldsymbol{b}}_n^\dagger(-\tau)\right) \ . \end{aligned} \quad \text{(A.8)}$$

For the transformation of the bosonic creation and annihilation operators one can derive a differential equation

$$\begin{aligned} \frac{\mathrm{d}}{\mathrm{d}t}\hat{\boldsymbol{b}}_n^{(\dagger)}(-\tau) = \frac{\mathrm{d}}{\mathrm{d}t}\left(e^{-i\hat{H}_B\tau}\ \hat{b}_n^{(\dagger)}\ e^{i\hat{H}_B\tau}\right) &= -i\ e^{-i\hat{H}_B\tau}\ \left[\hat{H}_B, \hat{b}_n^{(\dagger)}\right]\ e^{i\hat{H}_B\tau} \\ = (-)i\ e^{-i\hat{H}_B\tau}\ \hat{b}_n^{(\dagger)}\ e^{i\hat{H}_B\tau} &= (-)i\omega_n\hat{\boldsymbol{b}}_n^{(\dagger)} \ , \end{aligned} \quad \text{(A.9)}$$

and solve it under the initial condition $\hat{\boldsymbol{b}}_n^{(\dagger)}(0) = \hat{b}_n^{(\dagger)}$. The solution to Equation A.9 is

$$\hat{\boldsymbol{b}}_n^{(\dagger)}(-\tau) = \hat{b}_n^{(\dagger)}e^{(-)i\omega_n\tau} \ , \quad \text{(A.10)}$$

leading to

$$\hat{\boldsymbol{B}}(-\tau) = \sum_n \kappa_n \sqrt{\frac{\hbar}{2m_n\omega_n}} \left(\hat{b}_n e^{i\omega\tau} + \hat{b}_n^\dagger e^{-i\omega_n\tau}\right) \ . \quad \text{(A.11)}$$

Now we can calculate the commutator $[\hat{B}, \hat{\boldsymbol{B}}(-\tau)]$:

$$\begin{aligned}
\left[\hat{B}, \hat{\boldsymbol{B}}(-\tau)\right] &= \sum_{n,k} \frac{\kappa_n \kappa_k}{2\sqrt{\omega_n \omega_k}} \left[\hat{b}_n^\dagger + \hat{b}_n, \hat{b}_k e^{i\omega_k \tau} + \hat{b}_k^\dagger e^{-i\omega_k \tau}\right] \\
&= \sum_{n,k} \frac{\kappa_n \kappa_k}{2\sqrt{\omega_n \omega_k}} \left\{ \left[\hat{b}_n^\dagger, \hat{b}_k\right] e^{i\omega_k \tau} + \left[\hat{b}_n, \hat{b}_k^\dagger\right] e^{-i\omega_k \tau} \right\} \\
&= \sum_{n,k} \frac{\kappa_n \kappa_k}{2\sqrt{\omega_n \omega_k}} \left\{ \delta_{nk} e^{-i\omega_k \tau} - \delta_{nk} e^{i\omega_k \tau} \right\} \\
&= \sum_{n} \frac{\kappa_n^2}{2\omega_n^2} \left\{ e^{-i\omega_k \tau} - e^{i\omega_k \tau} \right\} \\
&= -2i \sum_{n} \frac{\kappa_n^2}{2\omega_n^2} \sin \omega_n \tau
\end{aligned} \tag{A.12}$$

Since this is a constant $\langle [\hat{B}, \hat{\boldsymbol{B}}(-\tau)] \rangle = [\hat{B}, \hat{\boldsymbol{B}}(-\tau)]$. By introducing the reservoir spectral density

$$J(\omega) = \sum_n = \frac{\kappa_n^2}{2\omega_n} \delta(\omega - \omega_n) \ , \tag{A.13}$$

Equation A.12 may be written as an integral

$$\left\langle \left[\hat{B}, \hat{\boldsymbol{B}}(-\tau)\right] \right\rangle = -2i \int_0^\infty d\omega J(\omega) \sin \omega \tau \ . \tag{A.14}$$

Under Born approximation, the reservoir is in thermal equilibrium so that the density matrix can be written as

$$\overline{\rho}_B = \frac{e^{-\beta H_B}}{\mathrm{tr}\left(e^{-\beta H_B}\right)} = \frac{1}{Z} e^{-\beta H_B} \ . \tag{A.15}$$

A.2 Correlation Length calculation

The two-point equal time correlation function of the XY model in 2D is defined as

$$C(x, y) = \langle \vec{s}_{0,0} \vec{s}_{x,y} \rangle \ . \tag{A.16}$$

The brackets $\langle \cdot \rangle$ denote the ensemble average

$$\langle \vec{s}_{0,0} \vec{s}_{x,y} \rangle = \frac{1}{Z} \int \prod_i d\vartheta_i \vec{s}_{0,0} \vec{s}_{x,y} e^{-\beta H(\{\vartheta\})} \tag{A.17}$$

I don't know where you have this definition from but i guess you can calculate it like this in the case of discrete states. But in XY model we don't have discrete states?

For the 2D anisotropic Ising Model, we can write down the Correlation Function in the limit for large distances as

$$C(x,y) \sim \frac{f_{\gtrless}(\theta)}{r^{\vartheta_{\gtrless}}} e^{-r/\xi_{\gtrless}(\theta)} \qquad \text{with} \qquad r = \sqrt{x^2+y^2}\ . \tag{A.18}$$

With known Functions $f_{\gtrless}(\theta)$ and $\xi_{\gtrless}(\theta)$ depending on the angle of the correlation vector and the Temperature $T \gtrless T_c$. We also know from mean field theory that (No, we also know from KT and stuff that the correlation function decays exponentially above the critical temperature [39, 24])

$$C(x,y) \sim e^{-r(x,y)/\xi(x,y)}\ . \tag{A.19}$$

We hope that the correlation function of the XY model has a similar form and proceed.

This is the definition of the correlation length ξ. The correlation length is a measure for the lengthscale over which perturbations of a system relax in space.

We are mainly interested in the correlation lengths in the directions along and across the dimer row and therefore define the correlation functions in those directions as

$$C_\perp(x) = \langle \vec{s}_{0,0}\vec{s}_{x,0}\rangle \sim e^{-x/\xi_\perp} \qquad \text{and} \qquad C_\parallel(y) = \langle \vec{s}_{0,0}\vec{s}_{0,y}\rangle \sim e^{-y/\xi_\parallel}. \tag{A.20}$$

Consider the fourier transforms of $C_\delta(r)$

$$S_\delta(k) = \sum_r^{N_\delta - 1} C_\delta(r) e^{-2\pi i \frac{kr}{N_\delta}}\ , \tag{A.21}$$

with N_δ being the number of lattice sites in the direction of δ. Set now without loss of generality $\delta = \perp$ to obtain

$$\begin{aligned} S_\perp(k) = \sum_x^{N_\perp - 1} C_\perp(x) e^{-2\pi i \frac{kx}{N_\perp}} = \sum_x^{N_\perp - 1} \langle \vec{s}_{0,0}\vec{s}_{x,0}\rangle e^{-2\pi i \frac{kx}{N_\perp}} = \sum_x^{N_\perp - 1} \langle s^0_{0,0} s^0_{x,0}\rangle e^{-2\pi i \frac{kx}{N_\perp}} \\ + \sum_x^{N_\perp - 1} \langle s^1_{0,0}\ s^1_{x,0}\rangle e^{-2\pi i \frac{kx}{N_\perp}}. \end{aligned} \tag{A.22}$$

The ensemble average can be computed by a sum over an infinite lattice

$$\langle s^\kappa_{0,0} s^\kappa_{x,0}\rangle = \lim_{N_\perp\to\infty} \lim_{N_\parallel\to\infty} \frac{1}{N_\perp N_\parallel} \sum_{i=0}^{N_\perp} \sum_{j=0}^{N_\parallel} s^\kappa_{i,j} s^\kappa_{i+x,j}\ . \tag{A.23}$$

An approximation is possible by using a finite lattice with large dimensions N_δ. Inserting Equation A.23 into Equation A.22 and replacing the sum $\sum_x$ with a sum over $q = i + x$ yields

$$S_\perp(k) = \frac{1}{N_\perp N_\parallel} \sum_{\kappa,q,i,j} s^\kappa_{i,j} s^\kappa_{q,j} e^{-2\pi i \frac{k(q-i)}{N_\perp}} = \frac{1}{N_\perp N_\parallel} \sum_{\kappa,q,i,j} \left(\sum_{p=0}^{N_\parallel} \delta_{p,j} \right) s^\kappa_{i,j} s^\kappa_{q,p} e^{-2\pi i \frac{k(q-i)}{N_\perp}} \ . \quad \text{(A.24)}$$

In the second step we have inserted a productive one in the form of a sum over a Kronecker delta. The Kronecker delta can be written as a sum over complex exponentials

$$\delta_{p,j} = \frac{1}{N_\parallel} \sum_{l=1}^{N_\parallel} e^{2\pi i \frac{l(j-p)}{N_\parallel}} \ . \quad \text{(A.25)}$$

Inserting this representation into Equation A.24 gives

$$\begin{aligned} S_\perp(k) &= \frac{1}{N_\perp N_\parallel^2} \sum_l \sum_\kappa \sum_{q,p,i,j} s^\kappa_{i,j} s^\kappa_{q,p} e^{-2\pi i \frac{k(q-i)}{N_\perp}} e^{2\pi i \frac{l(p-j)}{N_\parallel}} \\ &= \frac{1}{N_\perp N_\parallel^2} \sum_l \sum_\kappa \left(\sum_{i,j} s^\kappa_{i,j} e^{2\pi i \left(\frac{ki}{N_\perp} + \frac{lj}{N_\parallel} \right)} \right) \left(\sum_{q,p} s^\kappa_{q,p} e^{-2\pi i \left(\frac{kq}{N_\perp} + \frac{lp}{N_\parallel} \right)} \right) \ . \end{aligned} \quad \text{(A.26)}$$

The expressions in the parentheses are the fourier transforms $\tilde{s}^\kappa_{k,l}$, or respectively the conjugated fourier transform, of the $s^\kappa_{i,j}$ lattice:

$$\begin{aligned} S_\perp(k) &= \frac{1}{N_\perp N_\parallel^2} \sum_l \sum_\kappa \left(\tilde{s}^\kappa_{k,l} \right)^* \tilde{s}^\kappa_{k,l} \\ &= \frac{1}{N_\perp N_\parallel^2} \left(\sum_l |\tilde{s}^0_{k,l}|^2 + \sum_l |\tilde{s}^1_{k,l}|^2 \right) \ . \end{aligned} \quad \text{(A.27)}$$

This way we can calculate $S_\perp(k)$ by calculating the 2D fourier transforms of the lattices $s^0_{i,j} = \cos\vartheta_{i,j}$ and $s^1_{i,j} = \sin\vartheta_{i,j}$. The analogue result is valid for $S_\parallel(k)$.

To eventually extract the correlation length, we consider again Equation A.24 and insert the asymptotic behavior of C_δ Equation A.20 to obtain

$$S_\delta(k) \sim \sum_r^{N_\delta - 1} e^{-|r|/\xi_\delta} e^{-2\pi i \frac{kr}{N_\delta}} = \frac{2\xi_\delta}{1 + 4\pi^2 \xi_\delta^2 k^2} \ , \quad \text{(A.28)}$$

showing that $S_\delta(k)$ behaves like a lorentzian function around $k = 0$. Calculating $S_\delta(k)$ by means of Equation A.27 and fitting to the lorentzian Equation A.28 yields ξ_δ as fitting parameter.

A.3 Error calculation on moving averages

An average $\overline{f}$ that is calculated by the means of Equation 5.7 has a non trivial relationship with it's variance $\sigma_{\overline{f}}$ [47] (appendix C). The reason for this is that $f(t)$ and $f(t+mdt)$ might be, and most probably are, correlated. This means that observables at different times are not independent of each other and therefore have to be treated accordingly.

As a reminder, the average $\overline{f}$ is calculated as

$$\overline{f} = f_T = \frac{1}{T}\int_0^T dsf(s) \ , \tag{A.29}$$

with T being the total time of the simulation or the the time interval we want to average over. To estimate the error on f_T we consider the variance of the average f_T ([21] appendix D, [3] (p. 438 ff))

$$\begin{aligned}\sigma_{\overline{f}}^2 &= \left\langle f_T^2 \right\rangle - \left\langle f_T \right\rangle^2 \\ &\approx \frac{1}{T}\int_{-\infty}^{\infty} \mathrm{d}t \ C_f(t),\end{aligned} \tag{A.30}$$

with $C_f(t)$ being the autocorrelation or time correlation function

$$C_f(t) = \langle f(s)f(s+t)\rangle - \langle f(s)\rangle^2 \ . \tag{A.31}$$

The step performed in Equation A.30 is valid in the limit of $T \gg \tau_C$, that the sampling time T is much larger than the characteristic decay time of the autocorrelation function τ_C. τ_C is defined as

$$\tau_C = \frac{1}{2}\int_{-\infty}^{\infty} \mathrm{d}t \ C_f(t)/C_f(0) \ . \tag{A.32}$$

So that we can express $\sigma_{\overline{f}}^2$ in terms of τ_C

$$\sigma_{\overline{f}}^2 = \frac{2\tau_C}{T} C_f(0) \ . \tag{A.33}$$

Looking at Equation A.31, we can see that $C_f(0)$ reduces to the variance of f

$$C_f(0) = \sigma_f^2 \ . \tag{A.34}$$

Rewriting $T = n_s\tau_s$ with n_s being the number of measured samples and τ_s being the time

between the samples, the variance of the mean $\overline{f}$ can be expressed as

$$\sigma^2_{\overline{f}} = \frac{2\tau_C}{\tau_s}\frac{\sigma^2_f}{n_s} \ , \tag{A.35}$$

revealing that the variance of $\overline{f}$ is by a factor of $\frac{2\tau_c}{\tau_s}$ larger than the naive approach of uncorrelated measurements would yield. Since it is practically not possible to integrate Equation A.31 from $-\infty$ to ∞, we approximate τ_c by

$$\tau_C \approx \frac{1}{2}\int_{-T/2}^{T/2} \mathrm{d}t \ C_f(t)/C_f(0) \ . \tag{A.36}$$

A.4 Soft- and Hardware

Table A.1: The details and version numbers to the used soft- and hardware are listed.

Tool	Version number
Cuda	
cuRAND	11.2
cuFFT	
GCC	10.2.0
C++	C++17
Boost	1.78.0
OS	CentOS Linux 7.9.2009
CPU	Intel(R) Xeon(R) Gold 6148
GPU	Nvidia P100, V100

B Bibliography

[1] L Ts Adzhemyan, DA Evdokimov, M Hnatič, EV Ivanova, MV Kompaniets, A Kudlis, and DV Zakharov. The dynamic critical exponent z for 2d and 3d ising models from five-loop ε expansion. *Physics Letters A*, 425:127870, 2022.

[2] Karsten Ahnert, Denis Demidov, and Mario Mulansky. Solving ordinary differential equations on gpus. In *Numerical Computations with GPUs*, pages 125–157. Springer, 2014.

[3] Theodore W Anderson. *The statistical analysis of time series*. John Wiley & Sons, 2011.

[4] Inder P Batra. Atomic structure of the si (001)-(2× 1) surface. *Physical Review B*, 41(8):5048, 1990.

[5] Ben Mills. Wikipedia. 2024. "silicon". the silicon atoms are replaced by own color gradients. dimerization arrows, coordinate system and lattice constant added. Retrieved from `https://en.wikipedia.org/wiki/Silicon`, 2024.

[6] VL314399 Berezinskii. Destruction of long-range order in one-dimensional and two-dimensional systems having a continuous symmetry group i. classical systems. *Sov. Phys. JETP*, 32(3):493–500, 1971.

[7] Kurt Binder. Finite size scaling analysis of ising model block distribution functions. *Zeitschrift für Physik B Condensed Matter*, 43:119–140, 1981.

[8] Kurt Binder. Monte carlo simulations in statistical physics. In *Statistical and Nonlinear Physics*, pages 85–97. Springer, 2022.

[9] HWJ Blote, Erik Luijten, and Jouke R Heringa. Ising universality in three dimensions: a monte carlo study. *Journal of Physics A: Mathematical and General*, 28(22):6289, 1995.

[10] Christian Brand, Alfred Hucht, Giriraj Jnawali, Jonas D Fortmann, Björn Sothmann, Hamid Mehdipour, Peter Kratzer, Ralf Schützhold, and Michael Horn-von Hoegen. Dimer coupling energies of the si (001) surface. *Physical Review Letters*, 130(12):126203, 2023.

[11] Christian Brand, Alfred Hucht, Hamid Mehdipour, Giriraj Jnawali, Jonas D Fortmann, Mohammad Tajik, Rüdiger Hild Björn Sothmann, Peter Kratzer, Ralf Schützhold, and

Michael Horn-von Hoegen. Critical behavior of the dimerized si (001) surface: A continuous order-disorder phase transition in the 2d ising universality class. *arXiv preprint arXiv:2310.10488*, 2023.

[12] Axel Brünger, Charles L Brooks III, and Martin Karplus. Stochastic boundary conditions for molecular dynamics simulations of st2 water. *Chemical physics letters*, 105(5):495–500, 1984.

[13] Amir O Caldeira and Anthony J Leggett. Influence of dissipation on quantum tunneling in macroscopic systems. *Physical Review Letters*, 46(4):211, 1981.

[14] John Cardy. *Scaling and renormalization in statistical physics*, volume 5. Cambridge university press, 1996.

[15] DJ Chadi. Atomic and electronic structures of reconstructed si (100) surfaces. *Physical Review Letters*, 43(1):43, 1979.

[16] Jaroslaw Dabrowski and Matthias Scheffler. Self-consistent study of the electronic and structural properties of the clean si (001)(2x1) surface. *Applied Surface Science*, 56:15–19, 1992.

[17] B Dammann and JD Reger. Dynamical critical exponent of the two-dimensional ising model. *Europhysics Letters*, 21(2):157, 1993.

[18] Charlie Duclut and Bertrand Delamotte. Frequency regulators for the nonperturbative renormalization group: A general study and the model a as a benchmark. *Physical Review E*, 95(1):012107, 2017.

[19] Albert Einstein. Über die von der molekularkinetischen theorie der wärme geforderte bewegung von in ruhenden flüssigkeiten suspendierten teilchen. *Annalen der physik*, 4, 1905.

[20] Alan M Ferrenberg and DP Landau. Critical behavior of the three-dimensional ising model: A high-resolution monte carlo study. *Physical Review B*, 44(10):5081, 1991.

[21] Daan Frenkel and Berend Smit. *Understanding molecular simulation: from algorithms to applications*. Elsevier, 2023.

[22] Chu-Chun Fu, Mariana Weissmann, and Andrés Saúl. Molecular dynamics study of dimer flipping on perfect and defective si (001) surfaces. *Surface science*, 494(2):119–130, 2001.

[23] Daniel T Gillespie. The mathematics of brownian motion and johnson noise. *American Journal of Physics*, 64(3):225–240, 1996.

[24] S Grinstein. Renormalisation group analysis of the phase transition in the 2d coulomb gas, sine-gordon theory and xy-model. *Journal of Physics A: Mathematical and General*, 13(2):585, 1980.

[25] JD Guton, M San Miguel, and PS Sahni. Phase transitions and critical phenomena, vol. 8, 1983.

[26] Koichi Handa, Suminori Kono, Keijiro Saku, Jun Sasaki, Tomoki Kawano, Yasushi Sasaki, Tadayuki Hiroki, and Kikuo Arakawa. Plasma fibrinogen levels as an independent indicator of severity of coronary atherosclerosis. *Atherosclerosis*, 77(2-3):209–213, 1989.

[27] Martin Hasenbusch. The two-dimensional xy model at the transition temperature: a high-precision monte carlo study. *Journal of Physics A: Mathematical and General*, 38(26):5869, 2005.

[28] FJ Himpsel and DE Eastman. Photoemission studies of intrinsic surface states on si (100). *Journal of Vacuum Science and Technology*, 16(5):1297–1299, 1979.

[29] Pierre C Hohenberg and Bertrand I Halperin. Theory of dynamic critical phenomena. *Reviews of Modern Physics*, 49(3):435, 1977.

[30] J Ihm, DH Lee, JD Joannopoulos, and JJ Xiong. Structural phase diagrams for the surface of a solid: a total-energy, renormalization-group approach. *Physical review letters*, 51(20):1872, 1983.

[31] Kouichirou Inoue, Y Morikawa, K Terakura, and M Nakayama. Order-disorder phase transition on the si (001) surface: Critical role of dimer defects. *Physical Review B*, 49(20):14774, 1994.

[32] Jesús A Izaguirre, Daniel P Catarello, Justin M Wozniak, and Robert D Skeel. Langevin stabilization of molecular dynamics. *The Journal of chemical physics*, 114(5):2090–2098, 2001.

[33] HK Janssen, B Schaub, and B Schmittmann. New universal short-time scaling behaviour of critical relaxation processes. *Zeitschrift für Physik B Condensed Matter*, 73:539–549, 1989.

[34] Jorge V José, Leo P Kadanoff, Scott Kirkpatrick, and David R Nelson. Renormalization, vortices, and symmetry-breaking perturbations in the two-dimensional planar model. *Physical Review B*, 16(3):1217, 1977.

[35] Leo P Kadanoff. Scaling laws for ising models near t_c. *Physics Physique Fizika*, 2(6):263, 1966.

[36] Thomas WB Kibble. Topology of cosmic domains and strings. *Journal of Physics A: Mathematical and General*, 9(8):1387, 1976.

[37] Peter E Kloeden, Eckhard Platen, Peter E Kloeden, and Eckhard Platen. *Stochastic differential equations*. Springer, 1992.

[38] J M Kosterlitz and D J Thouless. Ordering, metastability and phase transitions in two-dimensional systems. *Journal of Physics C: Solid State Physics*, 6(7):1181, apr 1973.

[39] JM Kosterlitz. The critical properties of the two-dimensional xy model. *Journal of Physics C: Solid State Physics*, 7(6):1046, 1974.

[40] Masakazu Kubota and Yoshitada Murata. Streak patterns in low-energy electron diffraction on si (001). *Physical Review B*, 49(7):4810, 1994.

[41] Björn Ladewig, Steven Mathey, and Sebastian Diehl. Kibble-zurek mechanism from different angles: The transverse xy model and subleading scalings. *Physical Review B*, 102(10):104306, 2020.

[42] Pablo Laguna and Wojciech Hubert Zurek. Density of kinks after a quench: When symmetry breaks, how big are the pieces? *Physical Review Letters*, 78(13):2519, 1997.

[43] Erik Landemark, CJ Karlsson, Y-C Chao, and RIG Uhrberg. Core-level spectroscopy of the clean si (001) surface: Charge transfer within asymmetric dimers of the 2× 1 and c (4× 2) reconstructions. *Physical review letters*, 69(10):1588, 1992.

[44] Gabriel T Landi, Dario Poletti, and Gernot Schaller. Nonequilibrium boundary-driven quantum systems: Models, methods, and properties. *Reviews of Modern Physics*, 94(4):045006, 2022.

[45] L Larini, Riccardo Mannella, and Dino Leporini. Langevin stabilization of molecular-dynamics simulations of polymers by means of quasisymplectic algorithms. *The Journal of Chemical Physics*, 126(10), 2007.

[46] ZB Li, L Schülke, and B Zheng. Dynamic monte carlo measurement of critical exponents. *Physical review letters*, 74(17):3396, 1995.

[47] Neal Madras and Alan D Sokal. The pivot algorithm: A highly efficient monte carlo method for the self-avoiding walk. *Journal of Statistical Physics*, 50:109–186, 1988.

[48] M Matsumoto, K Fukutani, and T Okano. Low-energy electron diffraction study of the phase transition of si (001) surface below 40 k. *Physical review letters*, 90(10):106103, 2003.

[49] Daniel C Mattis. Transfer matrix in plane-rotator model. *Physics Letters A*, 104(6-7):357–360, 1984.

[50] Barry M McCoy and Tai Tsun Wu. *The two-dimensional Ising model*. Harvard University Press, 1973.

[51] N David Mermin and Herbert Wagner. Absence of ferromagnetism or antiferromagnetism in one-or two-dimensional isotropic heisenberg models. *Physical Review Letters*, 17(22):1133, 1966.

[52] AA Migdal. Phase transitions in gauge and spin-lattice systems. *Zh. Eksp. Teor. Fiz*, 69:1457, 1975.

[53] MP Nightingale and HWJ Blöte. Monte carlo computation of correlation times of independent relaxation modes at criticality. *Physical Review B*, 62(2):1089, 2000.

[54] NVIDIA, Péter Vingelmann, and Frank H.P. Fitzek. Cuda, release: 10.2.89, 2020.

[55] Lars Onsager. Crystal statistics. i. a two-dimensional model with an order-disorder transition. *Physical Review*, 65(3-4):117, 1944.

[56] Andrea Pelissetto and Ettore Vicari. Critical phenomena and renormalization-group theory. *Physics Reports*, 368(6):549–727, 2002.

[57] Devina Pillay, Brett Stewart, Chee Burm Shin, and Gyeong S Hwang. Revisit to the ising model for order–disorder phase transition on si (0 0 1). *Surface science*, 554(2-3):150–158, 2004.

[58] Renfrey Burnard Potts. Some generalized order-disorder transformations. In *Mathematical proceedings of the cambridge philosophical society*, volume 48, pages 106–109. Cambridge University Press, 1952.

[59] WH Press, SA Teukolsky, WT Vetterling, and BP Flannery. Numerical recipes in cþþ. *The Art of Scientific Computing, second ed., Cambridge University Press, Cambridge*, 2002.

[60] K Pyka, J Keller, HL Partner, R Nigmatullin, T Burgermeister, DM Meier, K Kuhlmann, A Retzker, Martin B Plenio, WH Zurek, et al. Topological defect formation and spontaneous symmetry breaking in ion coulomb crystals. *Nature communications*, 4(1):2291, 2013.

[61] A Ramstad, G Brocks, and PJ Kelly. Theoretical study of the si (100) surface reconstruction. *Physical Review B*, 51(20):14504, 1995.

[62] E Rastelli, S Regina, and A Tassi. Monte carlo simulation of a planar rotator model with symmetry-breaking fields. *Physical Review B*, 69(17):174407, 2004.

[63] Hannes Risken and Hannes Risken. *Fokker-planck equation*. Springer, 1996.

[64] VMH Ruutu, VB Eltsov, AJ Gill, TWB Kibble, M Krusius, Yu G Makhlin, B Placais, GE Volovik, and Wen Xu. Vortex formation in neutron-irradiated superfluid 3he as an analogue of cosmological defect formation. *Nature*, 382(6589):334–336, 1996.

[65] Gernot Schaller, Friedemann Queisser, Seyedeh Parya Katoorani, Christian Brand, Christian Kohlfürst, Mark R Freeman, Alfred Hucht, Peter Kratzer, Björn Sothmann, Michael Horn-von Hoegen, et al. Sequential kibble-zurek dynamics in the anisotropic ising model of the si (001) surface. *arXiv preprint arXiv:2310.18216*, 2023.

[66] Takeshi Tabata, Tetsuya Aruga, and Yoshitada Murata. Order-disorder transition on si (001): c (4× 2) to (2× 1). *Surface Science Letters*, 179(1):L63–L70, 1987.

[67] Thrust Development Team. Thrust: The c++ parallel algorithms library, 2023.

[68] Eite Tiesinga, Peter J Mohr, David B Newell, and Barry N Taylor. Codata recommended values of the fundamental physical constants: 2018. *Journal of Physical and Chemical Reference Data*, 50(3), 2021.

[69] Hiroshi Tochihara, Takaaki Amakusa, and Masashi Iwatsuki. Low-temperature scanning-tunneling-microscopy observations of the si (001) surface with a low surface-defect density. *Physical Review B*, 50(16):12262, 1994.

[70] RIG Uhrberg, GV Hansson, JM Nicholls, and SA Flodström. Experimental studies of the dangling-and dimer-bond-related surface electron bands on si (100)(2× 1). *Physical Review B*, 24(8):4684, 1981.

[71] S Ulm, J Roßnagel, G Jacob, C Degünther, ST Dawkins, UG Poschinger, R Nigmatullin, A Retzker, MB Plenio, F Schmidt-Kaler, et al. Observation of the kibble–zurek scaling law for defect formation in ion crystals. *Nature communications*, 4(1):2290, 2013.

[72] Robert A Wolkow. Direct observation of an increase in buckled dimers on si (001) at low temperature. *Physical review letters*, 68(17):2636, 1992.

[73] Chengcheng Xiao, Xinwei Wang, Xiaodong Pi, Shengyuan A Yang, Yuanping Feng, Yunhao Lu, and Shengbai Zhang. Spontaneous symmetry lowering of si (001) towards two-dimensional ferro/antiferroelectric behavior. *Physical Review Materials*, 3(4):044410, 2019.

[74] Wojciech H Zurek. Cosmological experiments in superfluid helium? *Nature*, 317(6037):505–508, 1985.

[75] Wojciech H Zurek. Cosmological experiments in condensed matter systems. *Physics Reports*, 276(4):177–221, 1996.

Erklärung

Hiermit erkläre ich, dass ich diese Arbeit im Rahmen der Betreuung am Institut für ??? Physik ohne unzulässige Hilfe Dritter verfasst und alle Quellen als solche gekennzeichnet habe.

Vorname Nachname
Dresden, Monat 2019